Investigation of Resonance States in ^{11}Li

by

Mukhwinder Singh

A Thesis Submitted to
Saint Mary's University, Halifax, Nova Scotia
in Partial Fulfillment of the Requirements for
the Degree of Master of Science in Applied Science.

in

August 2020, Halifax, Nova Scotia

Copyright Mukhwinder Singh, 2020

Approved: Dr. Rituparna Kanungo
Supervisor

Approved: Dr. Ian Short
Examiner

Approved: Dr. Greg Hackman
Examiner

Approved: Dr. David Hornidge
External Examiner

Date: 31st August 2020

Investigation of Resonance States in ^{11}Li

by Mukhwinder Singh

Abstract

Understanding the structure of complex many-body nuclei is one of the central challenges in nuclear physics. The conventional shell model is capable of explaining the structure of stable nuclei, but it starts to shatter towards the driplines or rare isotopes. To explain the new trends in the shell model at the driplines, it is essential to study these exotic nuclei. Halo nuclei are prime examples of some of the unusual characteristics of rare isotopes. In this study, we investigate the resonance states in the neutron dripline nucleus ^{11}Li through the deuteron scattering. The experiment was performed at the IRIS facility at TRIUMF with an ^{11}Li beam accelerated to 7.3A MeV. The thin windowless solid deuteron target was used as a deuteron source with two different thicknesses. Together with the ground state, multiple resonances are observed at 1.06 ± 0.06 MeV, 2.29 ± 0.04 MeV and 4.01 ± 0.04 MeV.

31st August 2020

Acknowledgement

Foremost, I would like to express my sincere thanks to my supervisor Prof. Rituparna Kanungo for her continuous support of my research, motivation, enthusiasm, and immense knowledge. It was a great privilege and honor to work and study under her guidance. Sincere gratitude to my thesis committee members Prof. Ian Short and Prof. Greg Hackman for their support throughout my research.

Thanks to everyone at TRIUMF especially Dr. Martin for all the help during the experiment. Thanks to Dr. Matthias Holl, Dr. David Walter, Dr. Jonas Refsgaard, Dr. Preetinder Jassal for all the discussions and suggestions during meetings.

Thanks to everybody at Saint Mary's University. To John Gallant and Michael Dunlavy for all the learning and discussion during Lab and it was pleasured to work with you as Teaching Assistant. Thanks to Florence Woolaver for all the support with documentation throughout the academic years. To all my friends at graduate office. To Mathieu for all the help with all those tough assignments and discussions. To Pranav for all the great time we had at work and outside.

Finally, a huge thanks to my family. To my brother for all the emotional support. Thanks to my parents for always boosting my confidence, all the blessing and having faith on me.

Contents

List of Figures

List of tables

Chapter 1

Introduction

The nucleus in an atom possesses a complex structure. Since, nuclear mass consists of atoms that make up planets, stars, human beings and every other visible object in the Universe, it is essential to study the structure and properties of atomic nuclei. The atomic nucleus is a strongly interacting, many-body quantum mechanical system that exhibits a fascinating variety of shapes and excitation modes, from spherical to super-deformed. The study of nuclear structure attempts to explain properties of the atomic nucleus, such as nuclear mass, characteristic energy levels, radioactive decay modes and many more, and how these properties emerge from the strong nuclear interaction between the nucleons (protons and neutrons) that form the nucleus.

There are a number of experiments performed to probe the structure of atomic nuclei that provide guidance to develop different theoretical nuclear models [1-5]; however, there is not a single theoretical framework that can describe all atomic nuclei. The bright side is there are different models that provide us with information about the different properties of the nucleus. For example, the one of the most basic properties of a nucleus is its size. But, how does one measure something thousands of times smaller even than the atoms that make up the measuring instrument itself? In 1909 Rutherford, Geiger and Marsden did just that [6]. By scattering alpha particles from thin gold foils, they discovered that nuclei were some ten thousand times smaller than the atoms that contained them. Since then, the idea of ‘seeing’ inside atoms, and indeed inside the nuclei themselves, has

involved hitting them with a beam of particles to observe. how many bounce off and at what angles it scatter? How easily do the nuclei become excited or break up or transform into other species?

Figure 1.1 shows the chart of nuclei. In this chart, nuclei are arranged according to their nucleon number, with increasing proton number on the vertical axis and the neutron number on the horizontal axis. The different color of each square represents the lifetime of the nuclei, black squares are for the stable nucleus (also known nuclei at stability line). Moving away from stability line, nucleon separation energy decreases, approaching zero at the driplines (extreme ends on the nuclear chart). The thick blue lines are drawn according to "*magic numbers*" i.e. 2, 8, 20, 28, 50, 82 and 126. The nuclei with these number of nucleons have higher average binding energy per nucleon than predictions from the semiempirical formula, hence more stable for any nuclear decay. The shell model explained the concept of magic number. The concept of shell model is similar to the atomic shell theory. According to the atomic shell theory, electrons in atoms are occupying discrete shells in the space surrounding the atomic nucleus [7,8]. Similarly, the nuclear shell model [9,10] states that the nucleons in nucleus are distributed in discrete shells. When the shell is completely filled the nuclei tend to have exceptional stability. The number of nucleons required to form a closed shell are referred to as magic numbers. Each shell represents a discrete energy value (Section 1.2).

The shell model was quite successful in explaining the closed shells; however, it was not able to explain all the features at nuclear limits (at driplines). These limits show different phenomena due to extreme neutrons-to-protons ratio and very low binding energy. In many cases, it is necessary to adopt different models altogether.

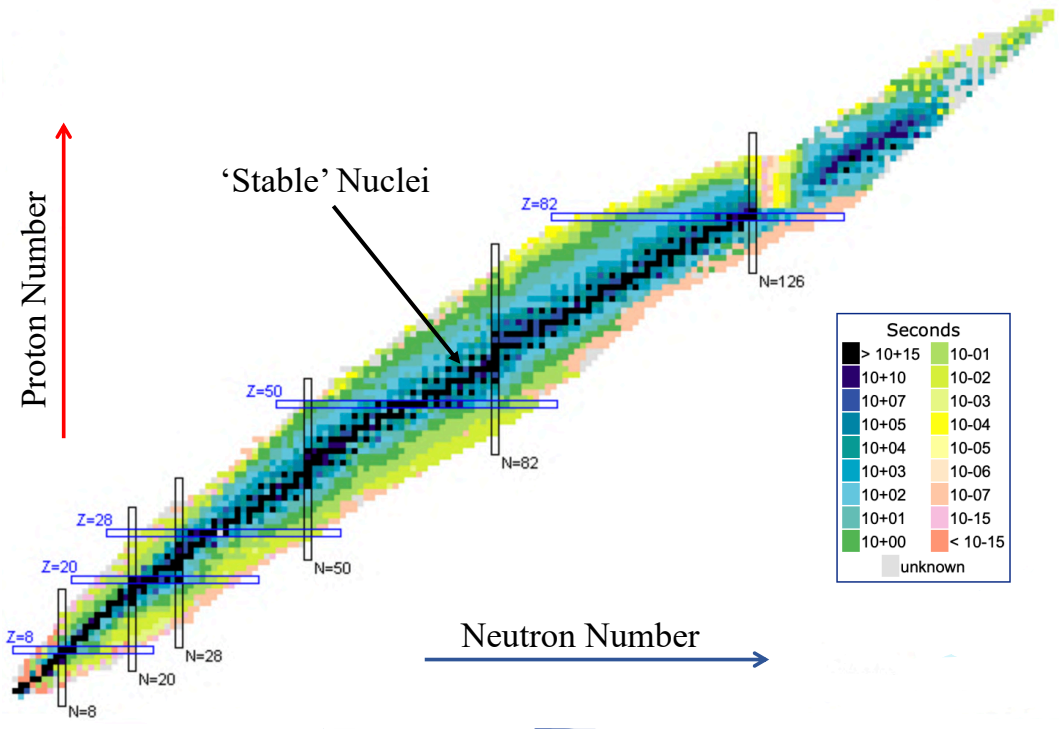

Figure 1.1 Chart of nuclei. The colour code indicates the decay lifetime (description in box). Magic number in N and Z are marked by blue lines. Data taken from the National Nuclear Data Center at Brookhaven National Laboratory [11].

To understand these exotic structures that appear at nuclear boundaries, it is of extreme interest to do experimental investigations of these nuclei. This thesis work concerns a particular feature usually formed in light, weakly bound systems: the *nuclear halo*.

1.1 The idea of halo system

The word halo is generally used to describe moon or sun halo. In general, a halo is any extended peripheral distribution around a central object. Similarly, in nuclear halo, the nuclear matter is spatially extended to significantly larger sizes than expected from theory. The halo nuclei consist of a core that is surrounded by a halo of orbiting protons or neutrons. These extended nucleons are very weakly bound to the rest of the nucleus. The halos were mostly identified in neutron-excess nuclei i.e. towards the neutron dripline. The proton

halos have been suggested in some experimental studies; however, the existence of proton halo is not as favorable as neutron halo due to the Coulomb barrier.

For stable nuclei, the nucleon separation energy is in the range of 6-8 MeV. However, in halo nuclei, the separation energy of last bound nucleon becomes very small (in some nuclei its even less than 1 MeV). The halo nucleus is a very loosely bound system and shows an extremely long tail in the neutron density distribution making the radius of nucleus much larger than expected [12].

To further understand halo phenomena, let's assume a system (nucleus) with an inert core and a loosely bound neutron with a square well interaction potential [13] of similar size as that of the core. The external wave function of the neutron is defined as

$$\psi(r) = \sqrt{\frac{k}{2\pi}} \frac{exp\,(-kr)}{r} \left[\frac{exp\,(kR)}{(1+kR)^{1/2}}\right] \qquad (1.1)$$

where R is width of potential well, k is decay parameter and related to separation energy E_s by:

$$k = \frac{\sqrt{2\mu E_s}}{\hbar}$$

where μ is reduced mass of system. With the decrease in E_s, the tail of matter distribution becomes longer.

There are two-neutron halo systems like ^{6}He and ^{11}Li. These systems with an even number of neutrons are particularly interesting. The strong force is unable to form a bound 2-n system, or to bind neutron to the core and therefore it cannot be treated as perturbation.

These systems are known as Borromean systems corresponding to Borromean rings. It is important to emphasize that although the density of a neutron halo is very low, it still strongly affects experimental observables such as the interaction cross-section. This fact was crucial in leading to the discovery of new properties in such nuclei.

There are few known halo nuclei so far. ^{6}He, ^{11}Li, ^{11}Be, ^{14}Be, ^{17}B, ^{15}C, ^{19}C, ^{22}C, ^{29}F and ^{37}Mg are neutron halo and ^{8}B, ^{13}N, ^{17}Ne, ^{26}P and ^{27}S are proton halo [14-27]. The size of a halo nucleus is significantly larger than its neighbouring isotopes. All the halo nuclei lie near driplines because here the separation energy is usually very small, which is the primary condition to form a halo nucleus. As the separation energy decreases the radius of nuclei become larger and larger and the radius diverges when the separation energy approaches zero for lower angular momentum (l) orbitals i.e. s- ($l = 0$) and p-($l = 1$) orbitals. On the other hand, the radius converges to certain values for d-wave ($l = 2$). This is true also for larger l orbitals. Therefore s-, and p-orbitals behave differently from other orbitals of larger l. That is one of the reasons why the halo phenomena associated with a low angular momentum orbital is interesting [28]. Figure 1.2 shows the positions of a few light halo nuclei in the chart of nuclides along with nuclei of interest for this thesis; ^{11}Li shown as a red square.

1.1.1 Evidence of halo nuclei

One of the achievements of Radioactive Ion Beams (RIBs) is the discovery of halo nuclei. It was first observed in 1985, when Tanihata and his group carried out an experiment to measure the sizes of lithium and helium isotopes [29]. In this experiment, the primary

beams of ^{11}B and ^{20}Ne at 800 MeV/nucleon were used to produce He and Li isotopes by projectile fragmentation with a Be target. The secondary beams of He and Li isotopes were

Figure 1.2 Position of halo nuclei in chart of nuclides [11]

led towards Be, Al and C reaction targets with energy of 790 MeV/nucleon. The corresponding interaction cross-section was measured to find the radius of the respective nuclei. The interaction nuclear radius was deduced from:

$$\sigma_I = \pi[R_I(p) + R_I(t)]^2 \quad (1.2)$$

where $R_I(p)$ is the projectile and $R_I(t)$ is the target radius. The cross-sections obtained from different targets proved that the projectile radius is independent of target variation. This indicates the interaction nuclear radius is a well-defined experimental observable for nucleus. The values of R_I for the He isotopes were found to increase with the nucleon number faster than the radius expected from general expression $R=R_oA^{1/3}$ (where R_o is constant), which holds for stable nuclei. In addition, a surprisingly large value for the ^{11}Li nucleus was obtained. Figure 1.3 shows the radius of He, Li, Be and C isotopes. For ^{11}Li,

the results were interpreted as “suggesting a large deformation or a long tail in the matter distribution”. Two years later, a measurement of the ground-state spin and the magnetic moment [39] seemed to rule out the first possibility. At last, Hansen and Johnson [13] introduced the term “halo” by explaining the large radius of ^{11}Li in Tanihata’s experiment is due to low binding energy of the last neutron pair.

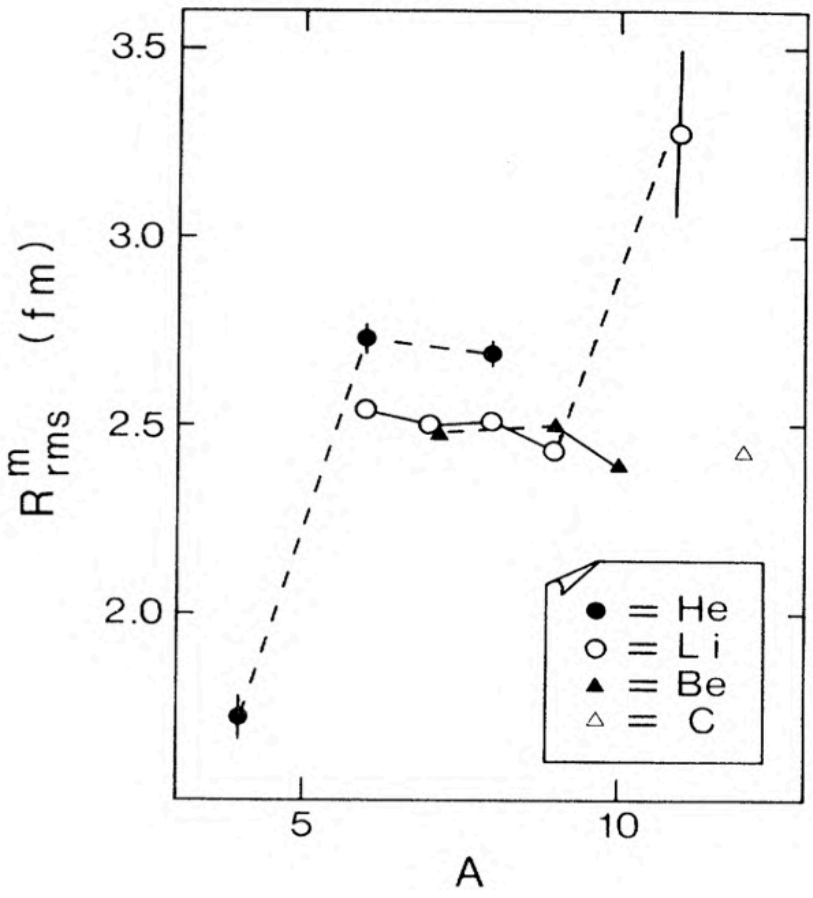

Figure 1.3 Root-mean-square matter radius extracted from calculations of interaction cross-section using a Glauber model and harmonic oscillators distributions for the densities of the particles. Lines connecting isotopes are only a guide for the eye [14].

There were further evidences of such type of nuclei observed by measuring the enhancement in cross section for electromagnetic dissociation, momentum distributions and β-decay [31-38].

1.2 Concept of excited states

There were many attempts to define the nuclear structure with a theoretical form. But as already mentioned the most successful so far is known as the shell model. The idea of shell structure in a nucleus was unbelievable at first, because a dense cluster of strongly interacting nucleons would be naively expected to crash into each other all the time, which would result in loss of energy of the particles. The basic explanation of nuclear energy states of the shell model is given by Pauli exclusion principle. According to this theory, all the lower energy nuclear states will fill up. This means particles cannot take part in the interactions which would decrease their energy, because there is no lower energy state accessible. Scattering from an external particle that increases the energy of nucleon can happen, but the scattering that lowers the energy is restricted by the exclusion principle [39].

The energy levels in any nuclei can be determined by its excitation spectrum. Each excited state is characterized by its angular momentum, parity and isospin (quantum numbers). The energy of these states depends upon the internal structure of the nucleus. The properties of these states can vary from one nucleus to another that can be measured by nuclear reactions and radioactive decays. These excited states can be bound or unbound. The unbound states are also known as resonance states.

A nucleus can be excited in different ways, e.g., by adding energy to a single nucleon or a collective excitation [40] (collective rotation or vibrations of all nucleons). The mode of excitation can be identified by measuring the cross-section and then comparing it to different models calculated by a single particle and a collective core excitation, to see which agrees best with experiment.

There have been various experiments to determine these excited states in each nucleus. For stable nuclei, the measurements are relatively easier than unstable ones, because we can form a long-lasting target for experiments with stable elements. However, for nuclei that lie far from the valley of stability with very short half-lives, it is not possible to form a stable target as they will decay. But with the development of new techniques, we can produce beams of these exotic nuclear species, which makes it possible to explore them.

1.3 Known properties of ^{11}Li

One of the most studied halo nuclei is ^{11}Li, a lithium isotope with eight neutrons and three protons and it consists of a core of ^{9}Li surrounded by two very weakly bound neutrons. The wavefunction of these two neutrons is spread out further in space than the core, which makes the size of ^{11}Li roughly the same as a lead nucleus, and lead has 208 nucleons. ^{11}Li has a half-life of 8.2 ms [41] for β^- decay with a matter rms radius found to be 3.27(24) fm [29]. As already mentioned, ^{11}Li is a two-neutron halo nucleus with a core of ^{9}Li, which has the remarkable property that none of its two-body subsystems are bound i.e. neither 2-*n* nor ^{10}Li is bound.

The ^{11}Li nucleus has only one observed bound state, the ground state with two neutron separation energy of ~369(65) keV [42]. However, there is evidence of resonances beyond this separation energy. The first effort to find the excited states of ^{11}Li was in 1992 by Kobayshi *et al.* [43], and study was done with the pion capture reaction ^{11}B $(\pi^-, \pi^+)^{11}$Li at T_π=164 MeV. The excitation energy peak structure apart from ground state was observed at 1.2 ± 0.1 MeV. However, there were no signs of higher resonances. The same experiment also hinted that the ^{11}Li is good candidate for soft giant dipole resonance at 1.2 MeV from

electromagnetic dissociation (EMD) measurements. There was no clear assignment of J^{π} values for this excited state.

Bohlen et al. [44] attempted to study excited states of ^{11}Li with two ^{14}C induced nucleon transfer reactions, ^{10}Be (^{14}C,^{13}N)^{11}Li and ^{14}C(^{14}C,^{17}F)^{11}Li, at 24 MeV/nucleon. The reaction products were detected by a combination of scintillator and gas filled chamber. The resonances were observed at 2.47(7) MeV, 4.85(7) MeV and 6.22(7) MeV. However, the background was high in both cases due to complex targets. None of these states were observed by Kobayashi[43] and the state observed at 1.2 MeV by Kobayashi was not seen in Ref. [44].

Another attempts to search for excited state were made at RIKEN in Japan [45]. The scattering of ^{11}Li+*p* was carried out at 74.5 MeV, where the beam of ^{11}Li was produced by the RIPS facility. The 11.75 mg/cm^2 or 9.5 mg/cm^2 thick target of CH_2 was used as a proton source. The scattered protons were detected by two solid state telescopes consisting of two silicon strip detectors and three silicon detectors. The excited states at 1.25(15) MeV, 3.0(2) MeV, 4.9(25) MeV, 6.4(2) MeV were observed. Only the state at 1.25 was statistically convincing, all higher states have very low statistics to distinguish as well-defined structure. Gornov et al. [46] observed the resonances at 1.02(7) MeV, 2.07(12) MeV and 3.63(13) MeV through the pion capture reaction, *^{14}C (π^-,pd)*. However, their data had very limited statistics for excited states and also poor resolution questioned the existence of these resonances.

There were other attempts [47-51] mostly focused on a resonance state near 1 MeV due to its soft dipole nature, which was successfully observed at 1.03(3) MeV with natural width of 0.51(11) MeV by Kanungo *et al.*[52] in 2015. The beam of ^{11}Li was reaccelerated at 5.5A MeV using the superconducting LINAC at TRIUMF and the experiment was

performed using solid D_2 target at the IRIS facility. A broad structure around 3.5 MeV was also observed but this structure was not statistically significant for further analysis. Figure 1.4 shows the summary of reported level scheme of ^{11}Li.

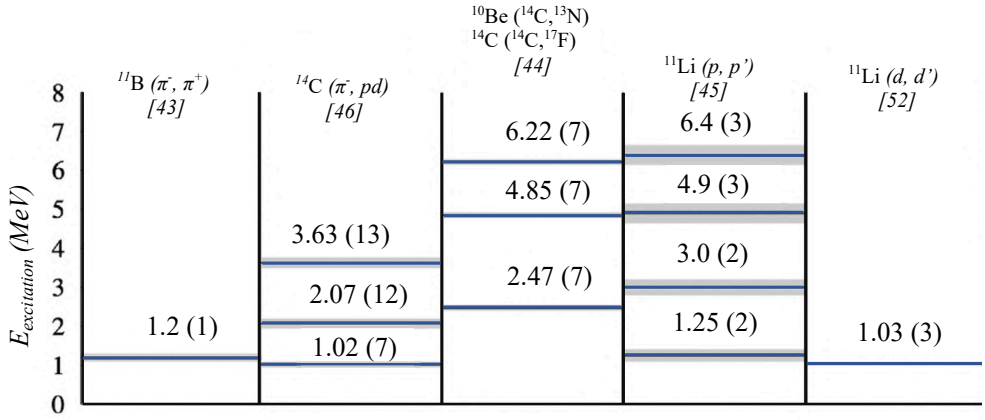

Figure 1.4 Reported resonance states of ^{11}Li. The grey bars are uncertainties in excitation energy [50].

It is clear from Figure 1.4 that the results in previous studies are contradictory above the first resonance state. The only agreement between Ref. [44] and [45] for states at 4.9 MeV and 6.4 MeV was seen within uncertainties. ^{11}Li is one of the most studied halo nuclei but still there are very few attempts to explore higher excited states of ^{11}Li.

The aim of this study is to investigate the resonance states of ^{11}Li through ^{11}Li *(d, d')* reaction. The primary focus is on excited states beyond the first excited state around 1 MeV because there is no conclusive knowledge on them.

The following is a brief description of the subsequent chapters.

- Chapter 2 gives an account of the experimental setup necessary for studying the ^{11}Li (*d,d*') reaction.
- Chapter 3 will discuss the techniques used in the analysis of the data from the experiment. It includes the calibration of required detectors, determining the solid

target thickness, particle identification, and counting and the incident beam particles.

- Chapter 4 will discuss and conclude the results obtained from the experiment.

Chapter 2

Experimental setup

A detailed discussion of experimental facility used to perform this study is presented in this chapter.

2.1 Production of Radioactive Ion Beam at TRIUMF

The radioactive ion beams play a very important role in understanding the properties of isotopes that have a proton to neutron ratio very different from stable isotopes in an unprecedented way. The production of these so-called exotic nuclei, however, is confronted with difficulties that stem from the

- extremely low production cross sections,
- overwhelming production of unwanted species in the same nuclear reaction,
- very short half-lives of the nuclei of interest.

Originally two complementary ways to make RIBs were developed: the isotope separation on-line (ISOL) technique and the in-flight separation technique. The basic requirements for the ISOL technique are: The primary beam, a target, mass separator and beam transport system. For the in-flight technique a multistage fragment separator is used instead of mass separator.

In our experiment, the beam of ^{11}Li was produced at ISAC facility of TRIUMF, Vancouver. At ISAC-II the RIBs are produced using ISOL technique [53]. In this technique, the exotic nuclei are produced by bombarding charged-particle beams or

neutrons on a sufficiently thick target. The reaction products are then transported into an ion source. After getting the desired charge state, the wanted species is obtained by electromagnetic separation. The various stages of beam production and delivery are schematically shown in figure 2.1.

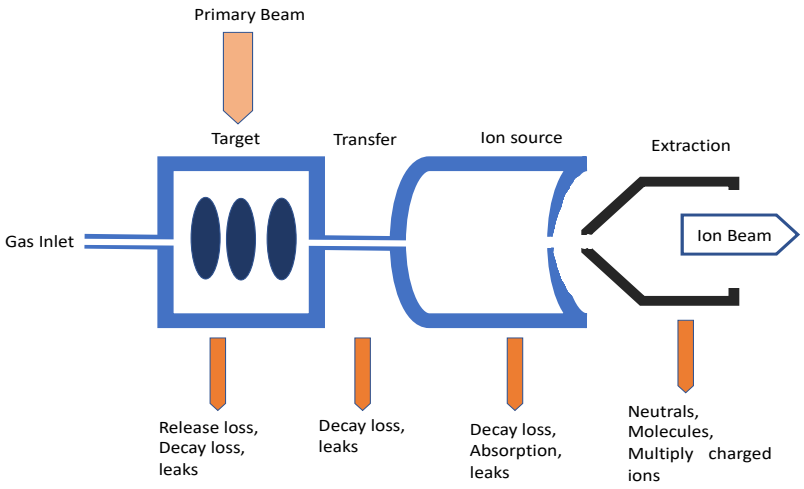

Figure 2.1 A schematic representation of the ISOL method and the major associated loss channels.

TRIUMF has the world's largest cyclotron, a source of 500 MeV protons used as the primary beam. This hits a tantalum target producing different fragments, which pour out into an ion source. A mass separator separates the ^{11}Li from other isotopes and then these low energy ^{11}Li particles are reaccelerated by using the ISAC-II superconducting linear accelerator to 7.3A MeV. This reaccelerated beam is then delivered to the experimental facility (IRIS).

2.2 IRIS

The ISAC Charged Particle Spectroscopy station (IRIS) is a facility stationed in the ISAC-II experimental area at TRIUMF. The primary focus of the IRIS facility is to study direct reactions such as transfer reactions, elastic and inelastic scattering in inverse kinematics. RIBs are the most commonly used beams. The rare isotope beams interact with

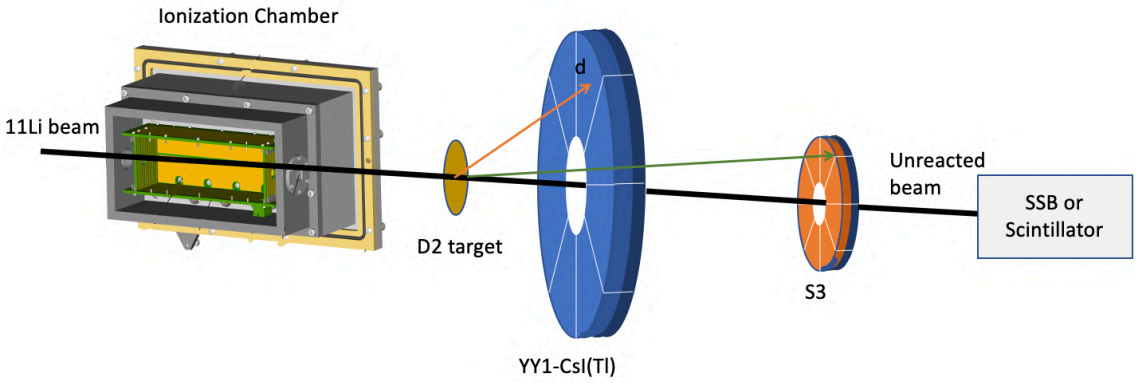

Figure 2.2 Schematic view of IRIS setup.

hydrogen (H_2) or deuterium (D_2) target. The charged particles produced from this interaction are collected and analyzed by different set of detectors. The main components of the IRIS assembly are

- Ionization Chamber (IC)
- Solid H_2 or D_2 target
- Charged particle detectors
- End detectors for detecting unreacted beam particles

Figure 2.2 shows the schematic view of the IRIS setup with all the major components.

2.2.1 Ionization Chamber (IC)

The first detector in the experimental setup is a low-pressure ionization chamber filled with isobutane gas. The pressure in the chamber is controlled and can be set to anywhere between 5 to 20 Torr. It enables us to determine the isobaric contaminants present in the beam. The beam enters and exits the IC through windows of 50 nm SiN_4 (silicon

nitride). These thin windows and the low pressure ensure the minimal energy loss and straggling in the ionization chamber. When a beam enters the ionization chamber it interacts with gas particles creating ions an electron pairs, which results in a loss of energy.

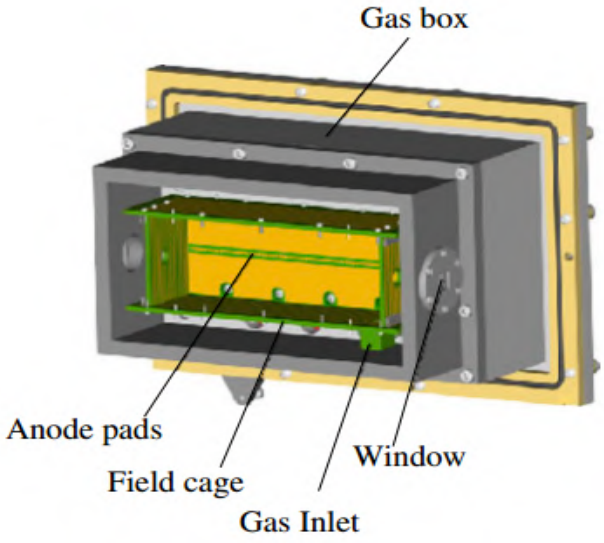

Figure 2.3 Layout of IRIS Ionization chamber

The electron and ion pairs are then collected by anode and cathode respectively, generating an electric signal at the anode. These electrical signals in the anode are read out with the help of preamplifiers. Figure 2.3 shows a schematic of the inside view of ionization chamber.

2.2.2 Windowless solid H_2/D_2 target

The special feature of IRIS is thin solid H_2/D_2 target. This windowless target is of paramount importance with RIB of weak intensity. The solid target has advantages over other targets like gas, liquid or polyethylene target. The solid target will have a higher density of target atoms available for reactions than gas or liquid. Therefore, the solid H_2 or D_2 target increases the reaction yield. The background scattering from carbon nuclei in

organic targets will not be present in case of solid H_2 or D_2 target. The assembly of solid H_2 or D_2 target is shown in figure 2.4. A hole of 5 mm diameter is bored at the center of a copper target cell. One surface of cell has a silver foil of 4.5 μm thickness affixed. This foil is used as a backing for the solid H_2 or D_2 target. The target cell is cooled to ~ 4 K using a cryocooler with a helium compressor. To minimize the radiative heating of the target; the

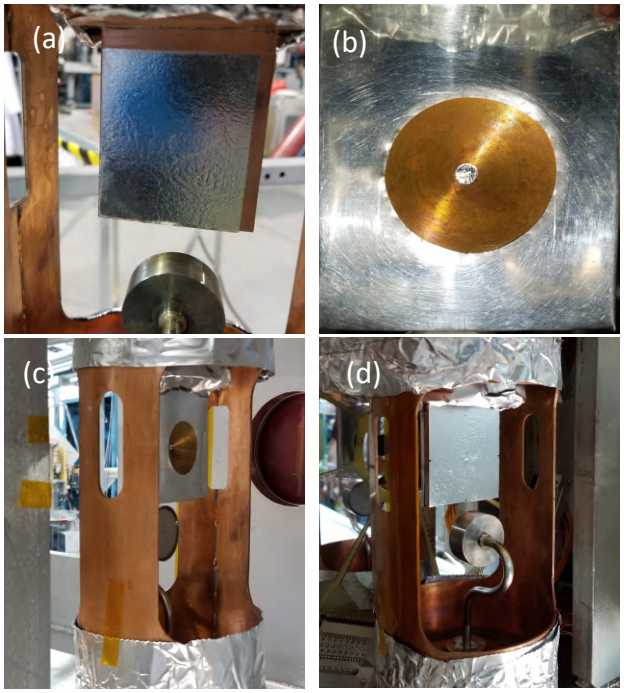

Figure 2.4 Solid D_2 target assembly. (a) Silver foil on copper cell. (b) View of copper cell. Copper cell placed inside the cylindrical heat shield c) front. d) back [54].

target cell has a cylindrical copper heat shield around it which is made up of oxygen free copper and is also cooled down to 24 - 27 K. When the target cell and shield reach their desired temperature, the diffuser is used to spray H_2 or D_2 gas on the surface of the silver foil. The diffuser is moved down from the beam line after the formation of target.

The incoming beam of ^{11}Li after traversing through the IC and the Ag foil interacts with the solid H_2/D_2 target. The reaction can take place anywhere within the target. The

reaction products go through the remaining thickness of the target after the interaction point. The background from Ag foil by fusion evaporation reactions can be separately measured by taking data without D_2 target.

2.2.3 Charged particle detectors

The IRIS facility is designed to detect the charged particle reaction products. To serve this purpose, the IRIS has two different set of detectors for detecting light target-like particles and heavy beam-like particles. Both sets have a combination of thin and thick detectors. The lighter particle passes through an array of 100 μm thick silicon strip detector (YY1 type) [55] , which is used to measure the energy loss and angle of the scattered particles. This array is made up of eight azimuthal sectors. Each of these sectors is segmented into sixteen rings. Each of these 128 segments act as an individual detector. These rings help to identify the angle of the detected particle. Depending upon the position of YY1 the array (figure 2.5 (a)), the angular range of detector can be calculated.

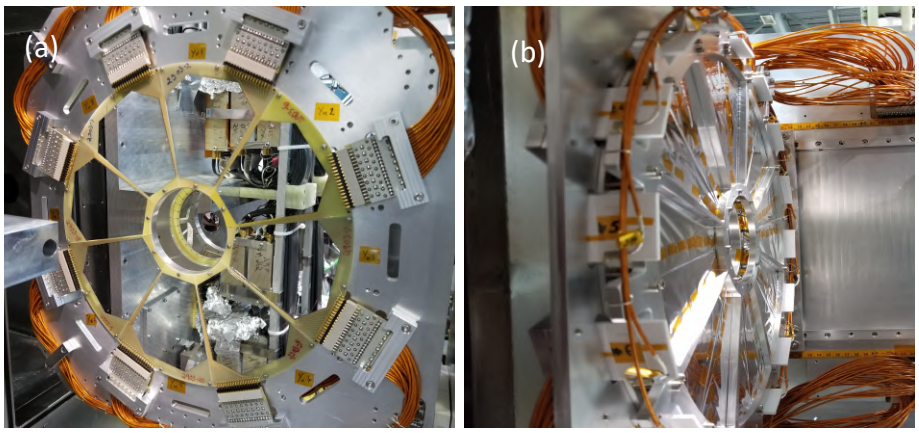

Figure 2.5 Detectors for target-like nuclei. (a) YY1 detector. (b) CsI(Tl) detector.

The lighter particles deposit part of their energy (ΔE) in YY1 and particle that do not stop in the YY1 detector array; deposit their remaining energy (E) in CsI(Tl) scintillator detector (figure 2.5 (b)) placed behind the YY1 detector array. The CsI(Tl) array is made up of 16 crystals each being 12 mm thick, arranged in same azimuthal configuration as the YY1 array. Two CsI(Tl) crystals matched with one sector of the YY1 detector. The YY1 and CsI(Tl) array are arranged in such a manner that they can detect target like particles in coincidence with each other. This combination also acts as ΔE-E telescope which allows particle identification.

The holes at the center of YY1 and CsI(Tl) detector arrays allow beam-like particles to pass through which are detected by a combination of thin and thick double-sided silicon strip detectors placed further downstream. These detectors are of S3 type [56] and identified as S3d1 followed by S3d2 (figure 2.6). The S3d1 is a thin (~60 μm) silicon detector used to measure energy and the scattering angle of beam-like scattered particles. It is segmented in 32 sectors on one side and 24 rings on the other side. The S3d2 is thick (~500 μm) silicon detector placed downstream to S3d1. It is also used to measure energy and angle of scattered heavy particles. The combination of S3d1 and S3d2 acts as a ΔE-E telescope for identification of beam like particles.

2.2.4 End detectors for the detection of unreacted beam particles

The detectors discussed above are annular in shape that allows the unreacted beam to pass through. The beam is stopped in radiation hard YAP:Ce inorganic scintillator. The signal of this scintillator is read out by a photomultiplier tube. This detector is used to count the number of unreacted beam particles. The ratio of particle counts in the ionization

chamber and the counts in the beam stopping scintillator helps to monitor the beam transmission ratio throughout the experiment. There is another zero-degree detector used to measure the remaining energy of unreacted beam after the target, which is a silicon surface barrier (SSB) detector. This also allows us to determine the formation and thickness of the D_2 target. Figure 2.7 shows an image of the SSB detector.

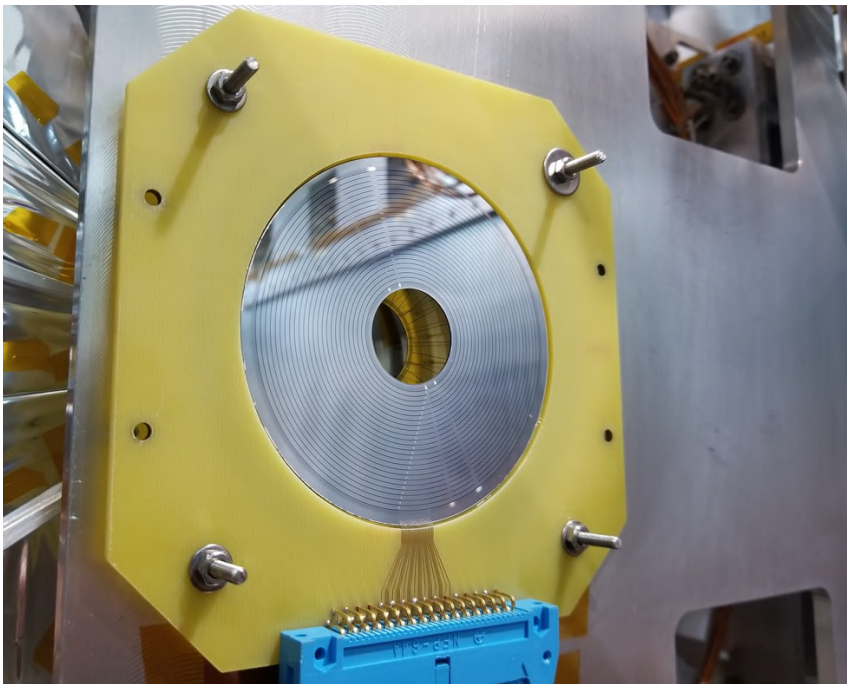

Figure 2.6 S3 detector

2.3 Signal processing

The interaction of a charged particles in the detectors produces a pulse of electric signal. This signal is then processed through preamplifier and shaping amplifier. The main purpose of the preamplifier is to extract a voltage pulse from the detector. These preamplifiers are located close to detectors to minimize any noise signal due to connecting cables. These preamplifiers are the charge sensitive type, which means the output voltage is proportional to the total integrated charge in the input pulse. The output pulse from

preamplifier has sharp rise time and slow decay time (figure 2.8(a)) governed by the time constant of the RC circuit. This output pulse is sent to a shaping amplifier for further amplification and pulse shaping. This pulse shaping process does not affect the maximum

Figure 2.7 SSB detector

amplitude of the pulse but reduces the pulse width. In general, the shaping amplifier unit involves a capacitor resistor (CR) network followed by few successive resistor-capacitor (RC) networks. The CR network blocks the low frequency component of signal, which improves the signal to noise ratio (SNR). High-frequency components are attenuated by RC network. We have used model MSCF-16 [57], a 16-channel shaper and timing amplifier with leading edge discriminator unit. The MSCF-16 has a built-in CR-RC network which amplifies and converts the preamplifier signal into a Gaussian pulse. The overlap between successive pulses is greatly reduced on converting the preamplifier pulse waveform into the Gaussian waveform. The discriminator unit of the MSCF-16 neglects the input signal with pulse height smaller than threshold value. The threshold value is adjusted to reject the pulses coming from the electronic noise. The discriminator (in the MSCF-16 unit) used in

this experiment was a leading-edge discriminator, whose purpose was to generate a trigger pulse at the moment the pulse crosses the threshold voltage level. The schematics of generating the shaped pulse and trigger signal are shown in figure 2.8(b).

To store the information presented in the pulse in useful form the signal is converted into digital form from analog. The amplified energy signal received from the pulse shaper unit goes into the analog-to-digital converter (ADC). This ADC unit converts the amplitude of an analog voltage signal into a proportional digital number. The ADCs (model number MADC32) employed in the experiment were of the peak-sensing type. These particular ADCs are 12 bits i.e. the full range is 4096 channels. Since we were interested in analysing the scattered particles detected with the YY1-S3 detectors, we performed a Logic-OR operation on the trigger signals obtained from the MSCF-16 unit of the YY1/S3 detectors. The obtained Logic- OR signal is called the "*free trigger*". The data acquisition system (DAQ) cannot store all the trigger events from the detectors because the DAQ system requires a finite amount of time to process an event. The accepted trigger is then fed into the Quad Gate generator unit (M794) to acquire the data in coincidence, which essentially generates a gate pulse with a user-defined time window (mostly 2 μs). This gate signal tells the ADC when to start and stop taking data.

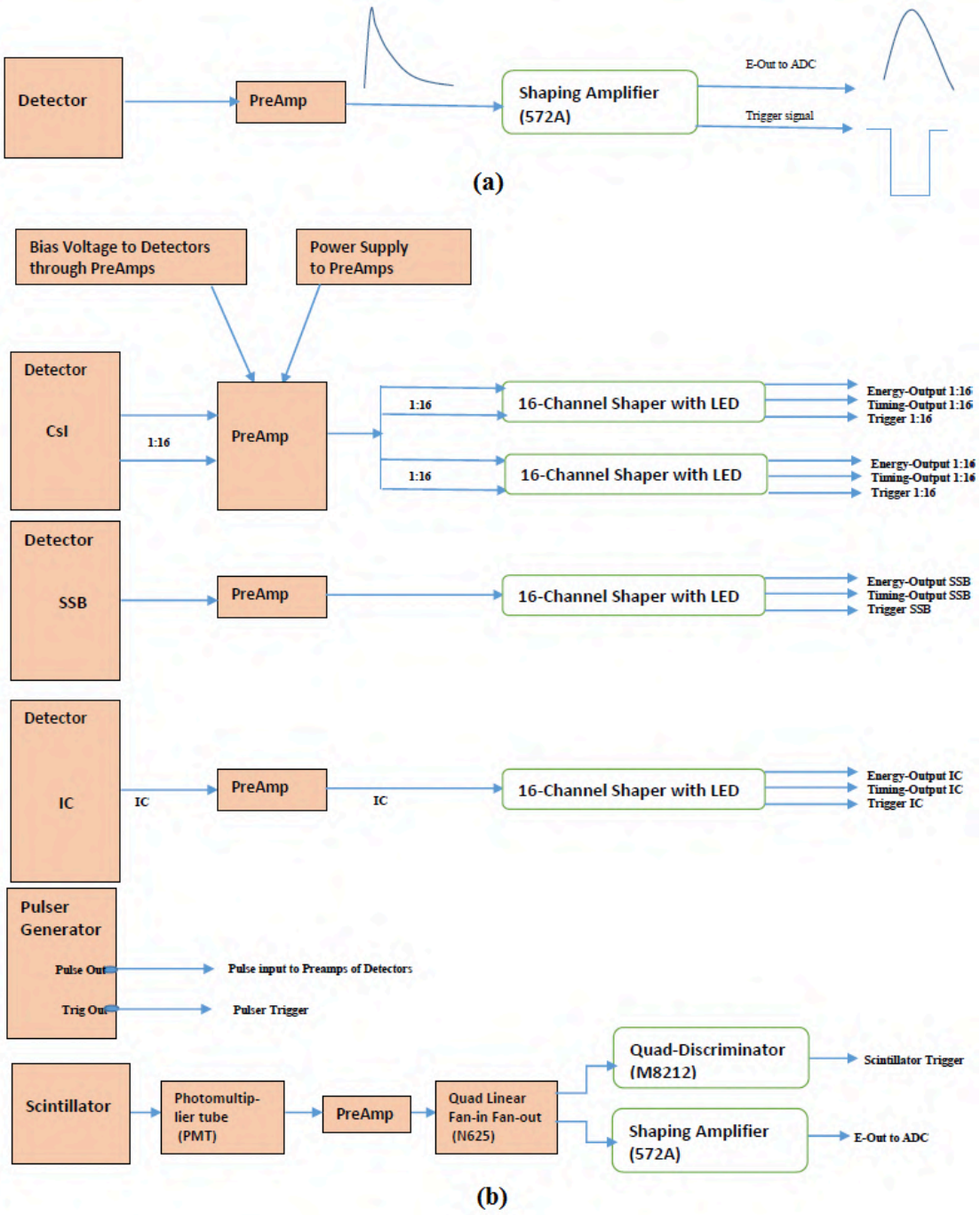

Figure 2.8 Pulse processing. (a) Output from a preamplifier unit and a shaping amplifier for a general detector. (b) Output from the shaping amplifier for CsI(Tl), SSB, IC, Pulser, and scintillator.

Chapter 3

Data Analysis

This chapter discusses the details of the data analysis. The first step is to identify any isobaric contaminant particles present in the beam. Following that, the discussion of calibration of the detectors required for the analysis is presented . It will also show how the solid D_2 target thickness has been measured throughout the experiment. Finally, the missing mass spectrum technique is discussed, for determining the excitation spectrum of ^{11}Li.

3.1 Identification of beam particles

The first step in analyzing the data was to identify the isobaric contaminants present in the beam. This was done by using the ionization chamber (IC) that was placed upstream of the target; it gives information about the atomic number of the particles present in the beam from the measured energy loss of the beam particles. The IC was operated with isobutane gas at 19.5 Torr throughout the experiment. The IC works on the principle of the stopping power of a charged particle passing through matter, which is defined as energy loss per unit length, and can be written as

$$-\frac{dE}{dx} \propto \frac{Z^2}{v^2} \qquad (3.1)$$

where v and Z are velocity and atomic number of the charged particle, respectively. The ADC spectrum of the IC detector is shown in Figure 3.1. From this spectrum, there is only

one Gaussian peak observed, which shows there was no isobaric contamination in the ^{11}Li beam.

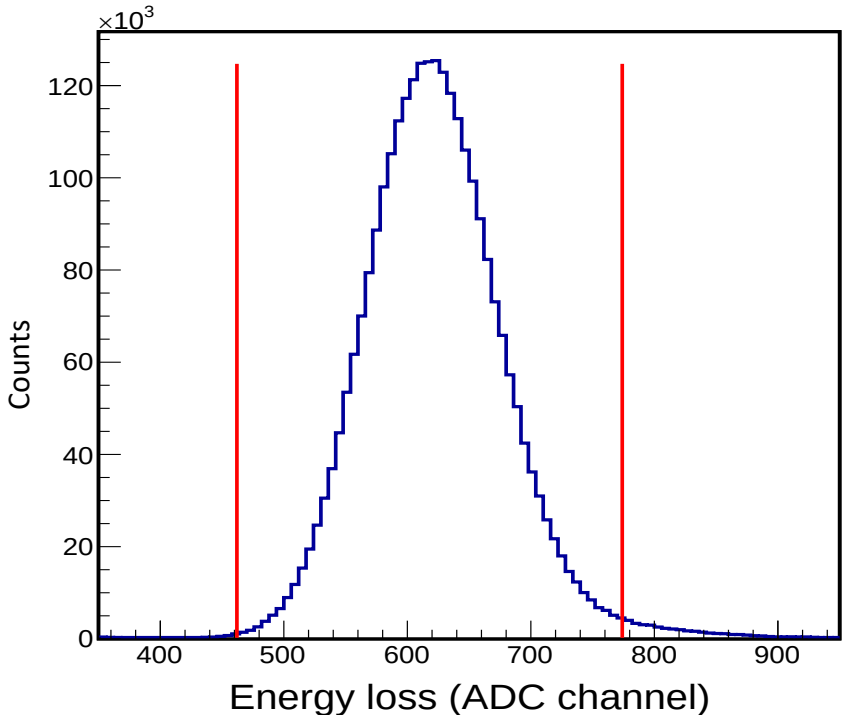

Figure 3.1 ADC spectrum of ionization chamber. Red vertical lines represent the 3σ selection region for ^{11}Li.

Even though the beam was pure ^{11}Li, the ADC channels between the red lines in Figure 3.1 were used for further analysis.

3.2 Detector Calibration

In this section, the detailed energy calibration of the detectors will be discussed. This energy calibration provides the base for the data analysis. As discussed previously, when a charged particle goes through a detector, it deposits its partial or complete energy and the detector generates a voltage pulse. This voltage pulse is converted into digital signal with help of a peak sensing ADC. This digital signal is in the form of channel number. The

basic meaning of the calibration is to convert the channel number into the more useful form i.e. energy. The following linear equation was used for the calibration of the detectors:

$$E = \mathrm{g} \times (c - p) \qquad (3.2)$$

where E is the energy deposited by an incoming charged particle in the detector, c is the peak position in channel number of the incident particle in the ADC spectrum, p is pedestals is a zero-energy point in the ADC spectrum (where the energy is measured to be zero), and g is a gain i.e. channel number to energy conversion factor for a particular detector spectrum. The unit of g is MeV/channel, if the energy deposited is in MeV. To calibrate a detector, determination of the gain and pedestals is required. The equation 3.2 describes the linear relation between the ADC channel number and the physical quantity energy. In this section, the discussion of the calibration of YY1, S3 and CsI(Tl) charged particle detectors is presented. The target thickness is necessary to calibrate the YY1 and CsI(Tl) detectors, hence it is also discussed in this section. The thickness of the Ag foil was 4.5 μm.

3.2.1 Calibration of S3d1 and S3d2 detector

In this section the calibration of the S3 detector is discussed. As mentioned in the previous chapter, the S3 detector telescope is a set of two detectors i.e. S3d1 and S3d2. Both the detectors required separate calibration but follow the same procedure. To calibrate the S3d1 detector, the experimental data obtained from elastic scattering of the ^{11}Li particles from the Ag foil was used. That means the data was collected without the D_2 target. The scattered ^{11}Li particles deposit part of their energy into S3d1 detector, while the

remaining energy is deposited in the S3d2 detector. Figure 3.2 shows the energy (channel number) deposited in the S3d1 detector versus the energy deposited in the S3d2 detector. The red polygon in the inset represents the selected events for elastically scattered ^{11}Li particles. The energy loss in the IC before the scattering was taken into account. The average probability of scattering location in Ag foil was taken at middle of foil thickness. The energy loss in all the dead layers of the S3 was also accounted for.

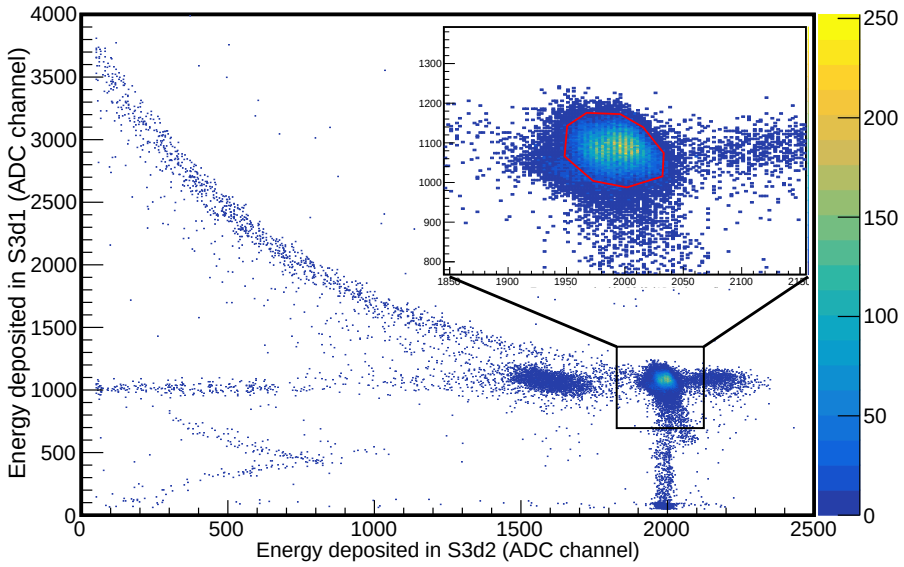

Figure 3.2 Energy deposited in S3d1 detector plotted against the energy deposited in S3d2 detector (ring side). The elastically scattered ^{11}Li region is zoomed. Elastically scattered ^{11}Li particles are selected by the red polygon in the inset.

As already discussed, both the S3d1 and S3d2 detectors have sectors on one side and rings on the other. The goal here is to find the gain for all the rings and sectors individually. For each of these rings or sectors, the ADC spectrum shows a peak (Figure (3.3)). Peak position of Gaussian fitting of the peak gave the channel number corresponding to the peak. The energy related to the peak for each ring was calculated using the scattering kinematics and taking the dead layer effects into account. Once the S3 detector is calibrated it can be used to find solid deuteron target thickness.

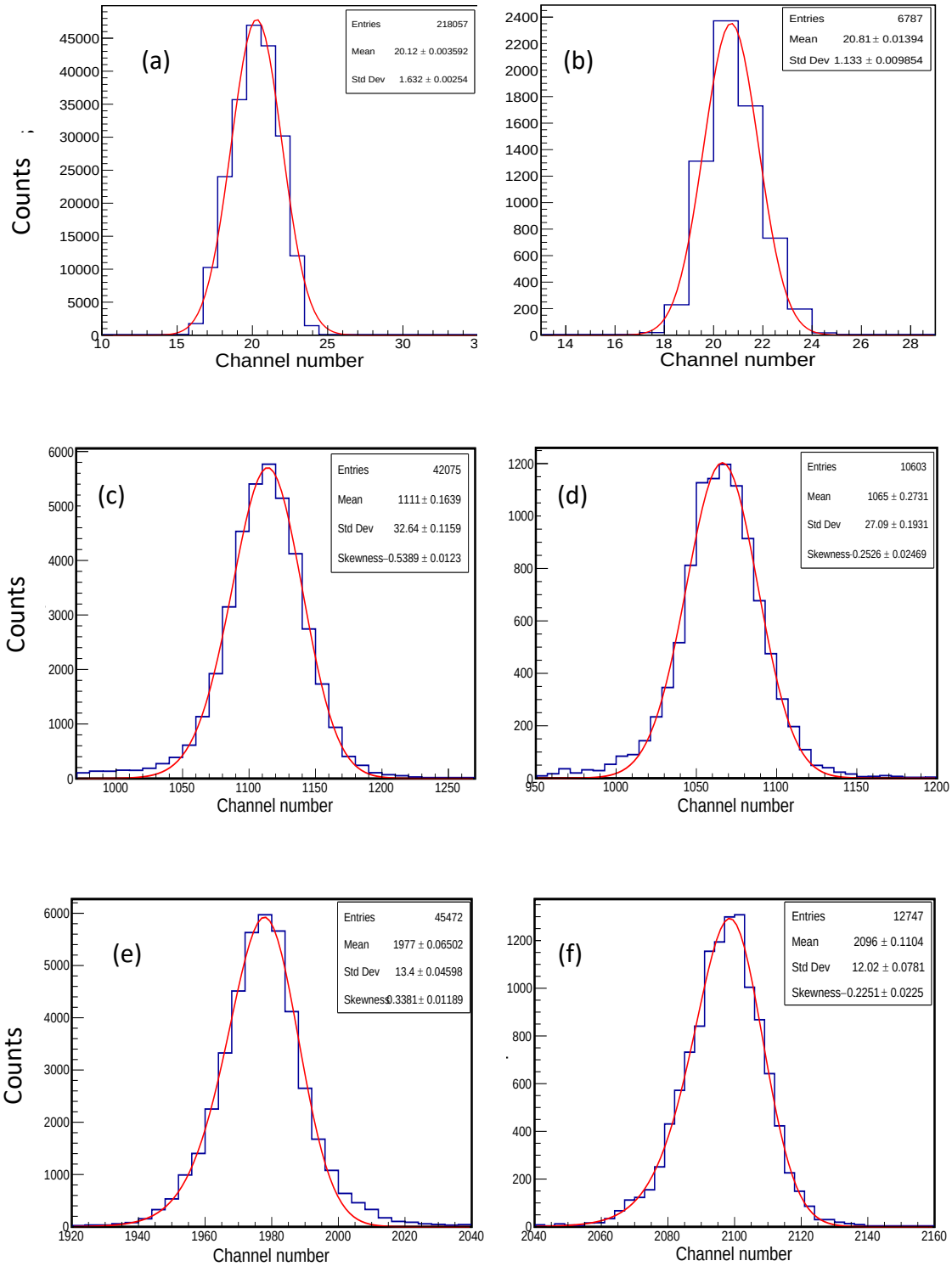

Figure 3.3 Histogram used for the calibration of the S3 detector. Pedestal data for the first ring of the (a) S3d1 detector and (b) of the S3d2 detector. Gaussian fitting of the ^{11}Li peak in the ADC spectrum of the (c) first ring of the S3d1 detector. (d) of the first sector of S3d1 detector. (e) of the first ring of S3d2 detector. (f) of the first sector of S3d2 detector. The data is without the solid deuteron target.

3.2.2 Determination of solid deuteron (D_2) target thickness

In this section the measurement of the solid D_2 target thickness will be discussed. The thickness was monitored throughout the experiment by using elastically scattered beam particles. This solid D_2 target thickness will also be necessary to calibrate the CsI(Tl) and YY1 detectors. To determine the target thickness, the elastic scattering of ^{11}Li particles from the Ag foil (^{11}Li(Ag,Ag)^{11}Li) with and without the D_2 target was used. The energy deposition of ^{11}Li particles with and without the deuteron target was measured in the first ring of S3d1 and S3d2 detector. The plot of total energy deposited in the S3 telescope is shown in Figure 3.4. The difference in energy with and without the D_2 target along with the stopping power was used to determine the thickness of solid D_2 target.

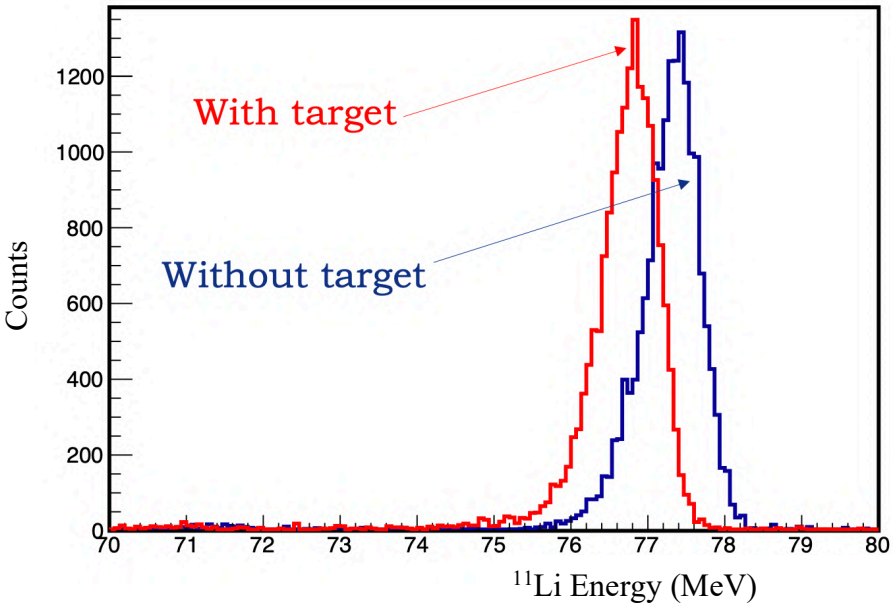

Figure 3.4 Energy deposited in S3 detector by elastically scattered ^{11}Li with (red) and without (blue) solid deuteron target.

Let us denote the ^{11}Li energy without the D_2 target by E_1 and energy measured after the D_2 target by E_2. Target thickness can be determined using following relation:

$$t = \int_{E_1}^{E_2} \frac{1}{S(E)} dE \qquad (3.3)$$

Where *S(E)* is stopping power of beam particles passing though the D_2 target that is given by *-dE/dx (*energy loss per unit length*), t* is the target thickness. In the determination of target thickness, the dead layers of the detectors were taken into account. Figure 3.5 shows the target thickness for each data collection set of 200 hours of duration. This target thickness was also verified with other rings of the S3 detector. The experiment was performed in two set of target thickness: with ~100 μm and ~50 μm thickness.

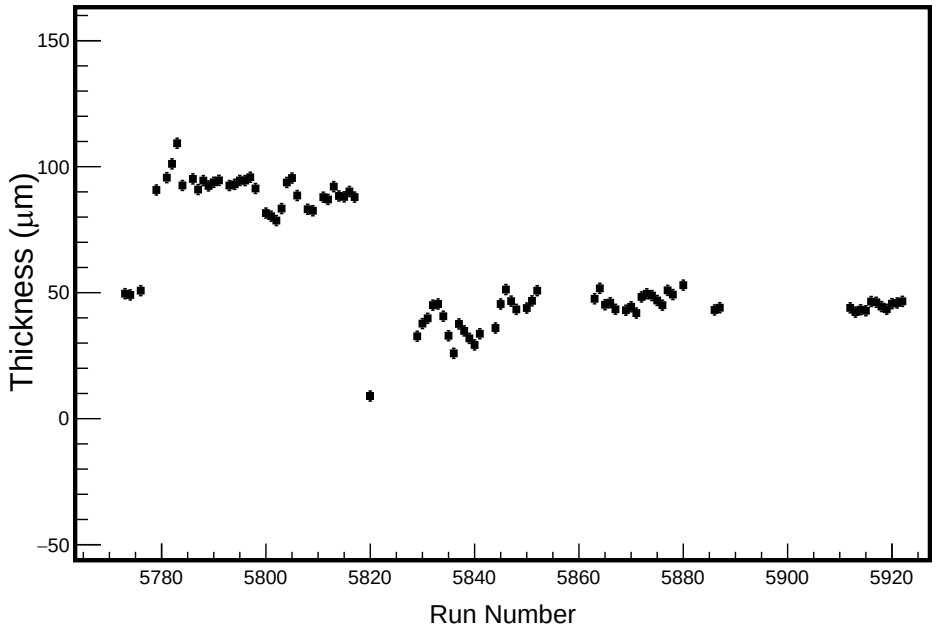

Figure 3.5 D_2 target thickness for each data run obtained with energy of ^{11}Li measured by the S3 detector.

3.2.3 Calibration of the YY1 array

The calibration of the YY1 silicon detector array can be done by two different methods at the IRIS setup. The first method is to use a standard alpha source and assign the known energies of this alpha particles to the ADC channel peak. The second method is to

use elastically scattered deuterons from the beam and assign the calculated energy for these deuterons from kinematic calculations to the corresponding channel number.

The initial calibration of the YY1 array was done by using the known triple-alpha source. The triple-alpha source was placed in front of the YY1 detector. The alpha source used for calibration has an isotope ^{239}Pu, ^{241}Am and ^{244}Cm emitting alpha particles of 5.155 MeV, 5.486 MeV and 5.805 MeV respectively, corresponding to the highest branching ratio. For each of these incident energies of the alpha particles, the energy losses in the dead layers of 0.1 μm Al and 0.05 μm Boron at respective angles were taken into account. The YY1 detector is thick enough to stop these alpha particles. The YY1 detector is segmented into 8 sectors and each sector has 16 rings, and each part is an individual detector making it a total of 128 channels for the entire array. Figure 3.6 represents the three peaks that correspond to the three different energies deposited by three different alpha particles. These peaks were fitted by the skewed gaussian function and the mean value of fitted the Gaussian was considered as the peak position. Each peak position gives the channel number related to the peak that correspond to the known triple-alpha energies. The gain of each channel was obtained by performing the least square fitting (Figure 3.7) to our calibration equation 3.2. The calibrated YY1 spectrum is shown in Figure 3.8.

To verify the calibrated energy, the comparison between the elastically scattered deuterons from solid D_2 target (^{11}Li*(d,d)*^{11}Li) to the expected energy deposited by the deuterons from kinematic calculations was done. The first step was to identify the deuterons which were elastically scattered from the target, to serve that purpose IRIS setup has a light

particle *ΔE-E* telescope. Figure 3.9 shows energy deposited in the YY1 detector versus energy deposited in the CsI(Tl).

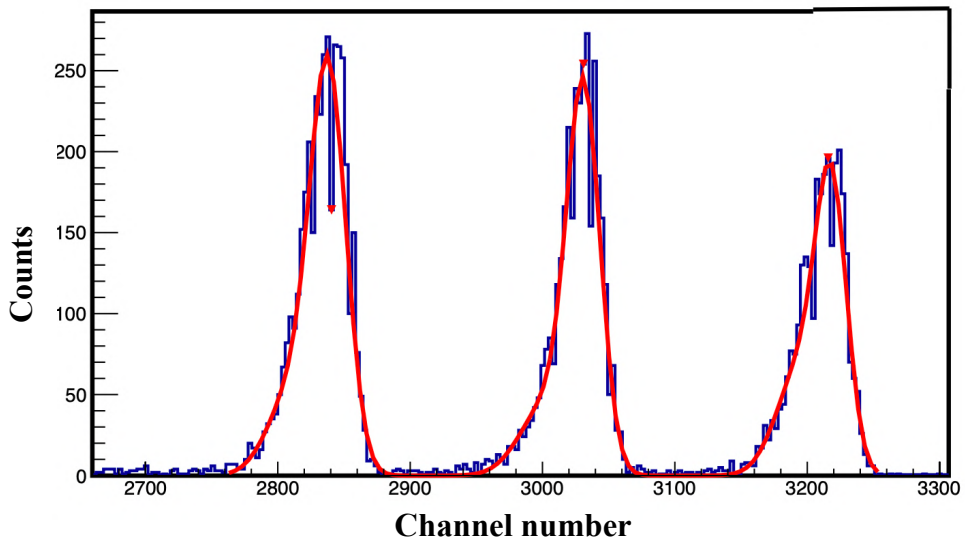

Figure 3.6 The YY1 spectrum for triple alpha source for one detector out of the 128 detectors.

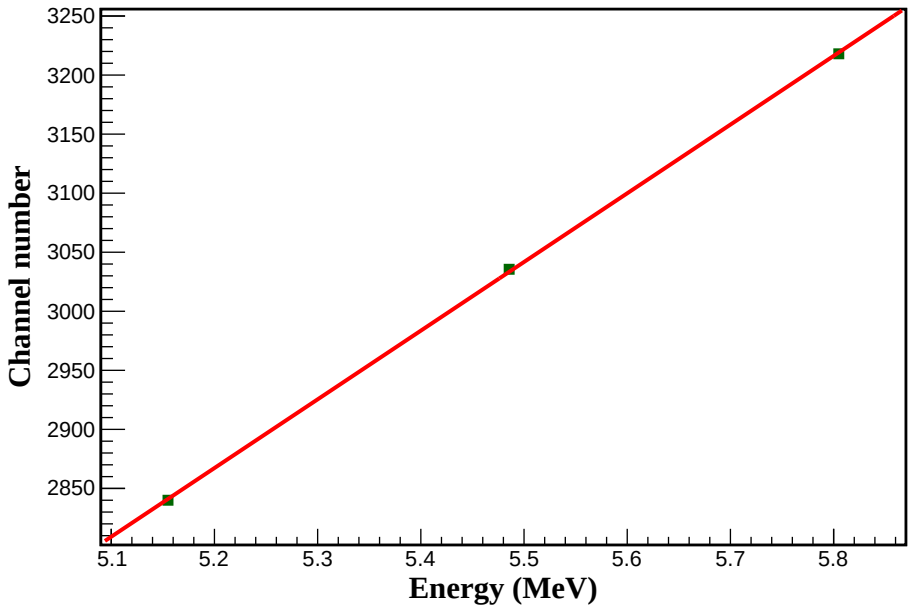

Figure 3.7 Least square fit using the equation 3.2 for YY1 detector.

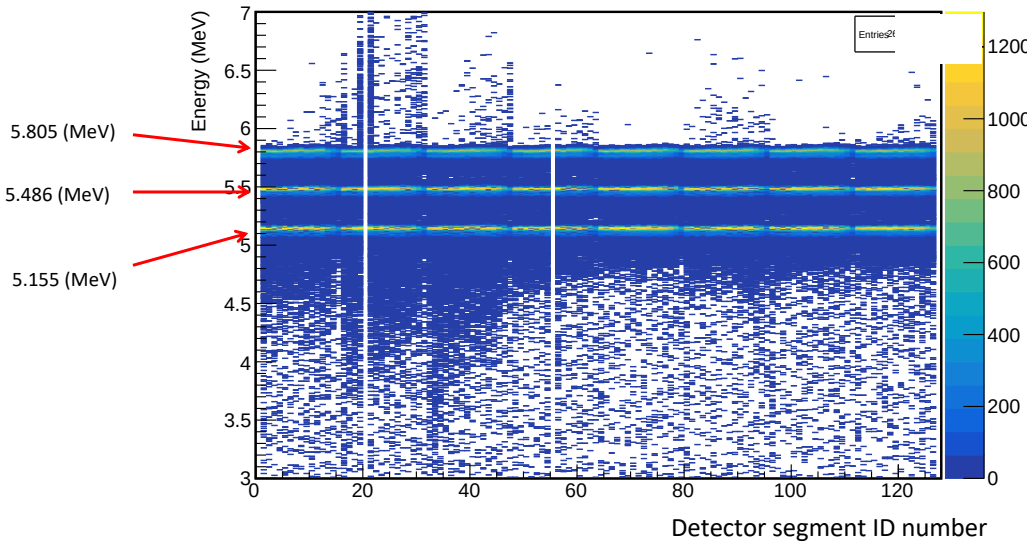

Figure 3.8 Calibrated YY1 spectrum as a function of different detector segments with the triple alpha source.

In order to eliminate kinematic shifts from different detector channels that may obscure the particle identification, the energy-loss is corrected for the scattering angle dependent effective thickness. The red polygon shows the selected events of the deuterons.

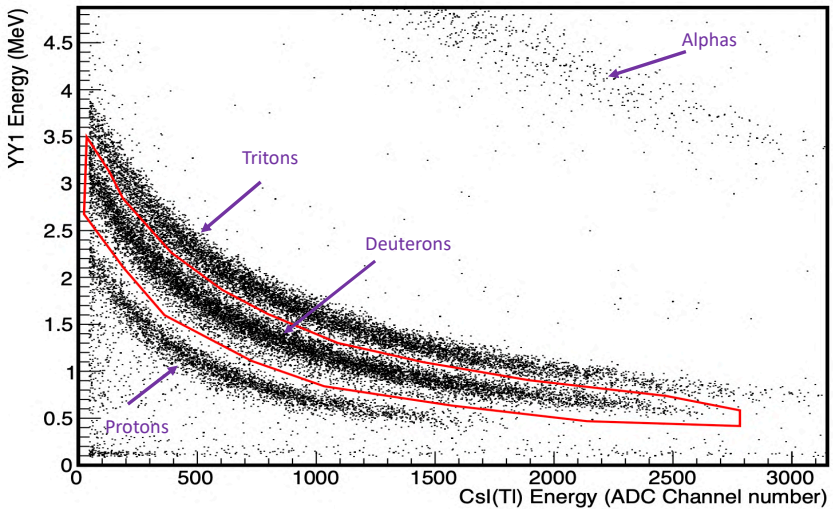

Figure 3.9 Light target-like particle identification by *ΔE-E* telescope.

This selection contains all the deuterons i.e. elastic as well as inelastic. To select only the elastically scattered deuterons the heavy particle *ΔE-E* telescope (S3 detector) was used.

Figure 3.10 shows the energy deposited in S3d1 vs S3d2 detector. The red polygon is drawn around the elastically scattered ^{11}Li. With the help of this selection, the deuterons in coincidence with elastically scattered ^{11}Li are the elastically scattered

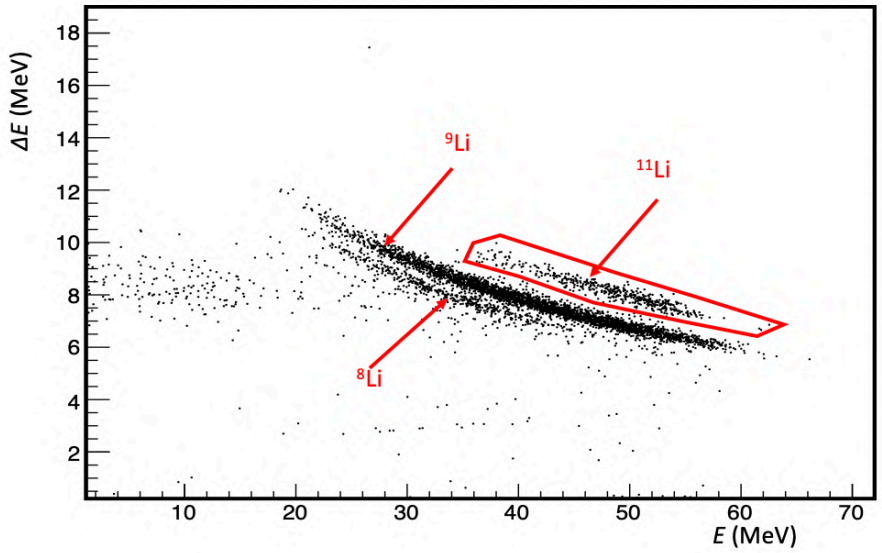

Figure 3.10 Heavy beam like-particle identification by S3 *ΔE-E* telescope.

deuterons. The calibrated energy-loss spectrum of the elastically scattered deuterons was compared with the simulated energy-loss spectrum for the reaction ^{11}Li*(d,d)* in Figure 3.11. The two spectra that are expected to be identical however they show some difference that is angle dependent. The possible reasons could be some corrections in the alpha source calibration or the determination of distance between solid D_2 target and YY1 detector.

To resolve this issue, the data from stable beam , ^{22}Ne that was collected using the same experimental setup just prior to the ^{11}Li(*d,d)* experiment was analyzed. The calculated energy-losses of the scattered deuterons from ^{22}Ne(*d,d*) were used to recalibrate the YY1 detector. It follows the same procedure used to calibrate the S3 detector in section 3.2.2. After recalibration of the YY1 detector, the elastic scattered deuterons from ^{11}Li*(d,d)*

reaction were compared again with the energies from kinematic calculations. However, this didn't resolve the issue of angle dependent discrepancy between them. This confirms the determination of distance between the target and YY1 detector likely requires some corrections.

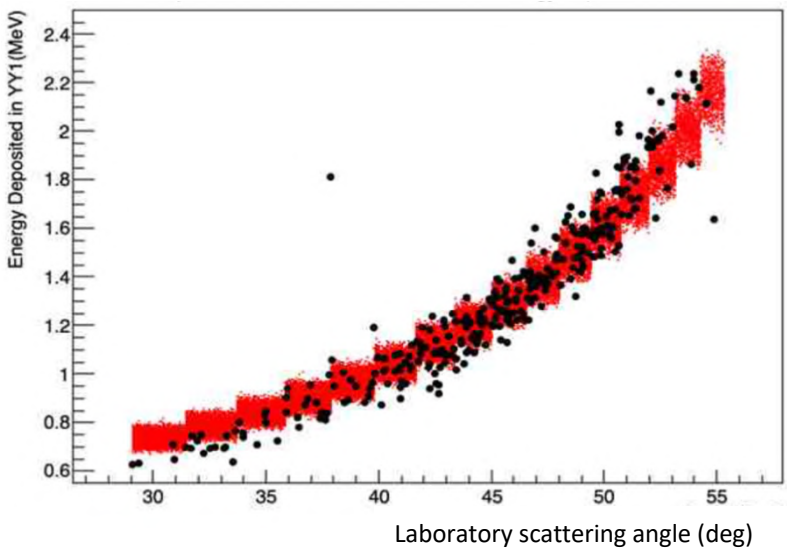

Figure 3.11 Energy deposited by elastically scattered deuteron vs laboratory angle. Red events show the simulated deuterons. Black dots correspond to observed deuterons from the ^{11}Li(*d,d*) data calibrated using ^{22}Ne(*d,d*).

3.2.4 Detector distance determination

The distance between the solid D_2 target and the YY1 detector was originally set to be 90 mm during the experiment. But as already discussed this distance did not consistently describe the simulation and the data. To determine the actual distance between the deuteron target and the detector, the calibration of YY1 detector was done for different distances. As first step, the detector was set to be at 80 mm distance from the target and calibrate with elastically scattered deuterons from ^{11}Li*(d,d)*^{11}Li reaction. Using this calibration, the measured energy of the deuterons from ^{22}Ne*(d,d)*^{22}Ne' was compared with the calculated

energy expected from the reaction kinematics. To get the best fit the overlap parameter was defined as

$$\text{overlap parameter} = \sum(n \times \log(n/y) + y - n) \qquad (3.4)$$

where y and n correspond to calculated and measured energy value of each event, respectively. This parameter gives the overlap between two 2-D histograms. This process was repeated for 83 mm, 85 mm, 87 mm and 90 mm distances. The fitted spectra for different detector distances vs the overlap parameter is shown in Figure 3.12. The minimum was observed at 85 mm. The YY1 detector then calibrated with elastically scattered deuterons from the ^{11}Li beam using this distance of minimum overlap parameter.

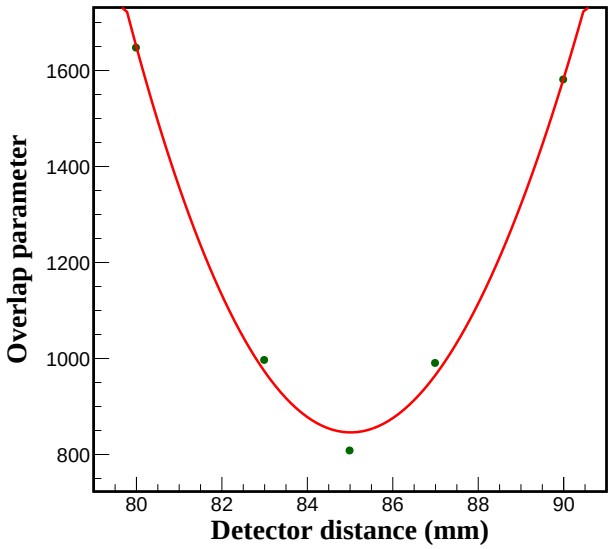

Figure 3.12 Overlap parameter vs detector distance from target fitted with 2nd degree polynomial.

3.2.5 Calibration of CsI(Tl)

The CsI(TI) detector array is composed of 16 unsegmented crystals. Calibration with an alpha source was not suitable since the pulse height maybe dependent on distance

of particle from readout photodiodes. Therefore, the elastically scattered deuterons from the target was used. The energies of the deuterons were determined by the same method as described in section 3.2.3.

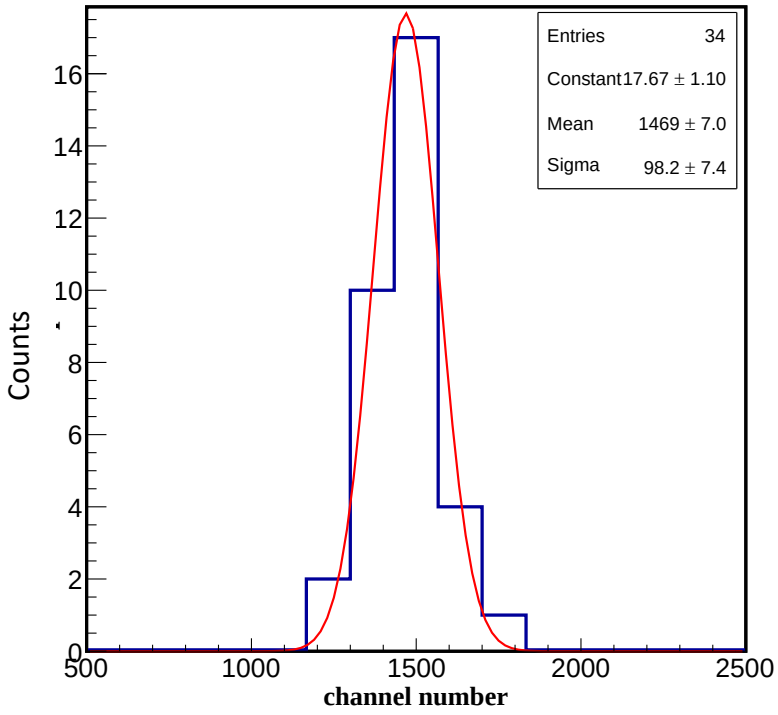

Figure 3.13 The ADC spectrum for ^{11}Li(*d,d*) for a CsI(Tl) crystal in coincidence with four rings of the matching YY1 sector.

The coincidence of the YY1 detector with the CsI(TI) provides a study of the position sensitivity of the pulse height and hence gain of CsI(Tl) crystals. There are 16 rings in each sector, the combination of 4 rings was taken at a time due to low statistics of the elastically scattered deuterons. For each of these combinations, the ADC spectrum shows a peak (Figure 3.13) which corresponds to the scattered deuterons. This ADC channel is then compared to the simulated energy for the corresponding angle bin to find the gain. A calibrated spectrum of the CsI(Tl) detector is shown in Figure 3.14. Calibration of each detector is also verified by using the data with stable beam ^{22}Ne.

3.3 Missing mass technique

After successful calibration of all the detectors. The excitation spectrum was generated by using the missing mass technique. First the Q value spectrum is generated that then converted into excitation spectrum. Q value is the amount of energy released or absorbed during any nuclear reaction. For a given reaction, $A + B \rightarrow a + b$, then Q value is defined as:

$$Q = m_A + m_B - m_a - m_b \qquad (3.5)$$

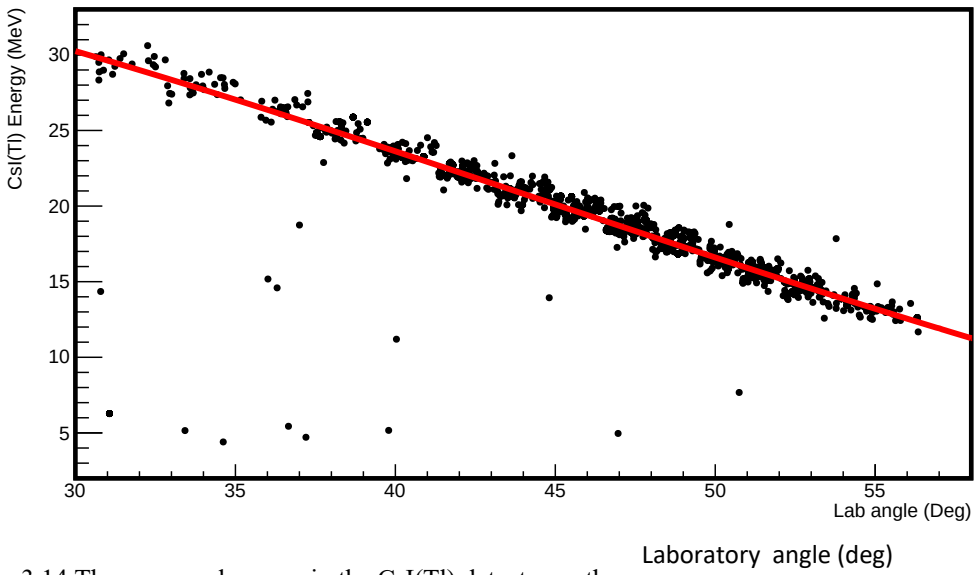

Figure 3.14 The measured energy in the CsI(Tl) detector vs the scattering angle of the deuterons for the ^{11}Li+d reaction. The red curve shows the calculated values.

If any of the reaction products (either a or b) are in an excited state, then the mass of the excited particle is different from its rest mass due to mass-energy equivalence. The mass of this excited particle can be determine by using the mass-energy and momentum conservation. Let's assume the particle "b" is in excited state, the mass of particle "b" can be written in the form of kinetic energies and scattering angles of the other product i.e. "a",

$$m_b = \sqrt{(m_A{}^2 - m_B{}^2 + m_a{}^2 + 2m_B(T_A + m_A) - 2(T_A + m_A + m_B)(T_b + m_a) + 2P_A P_a \times \cos(\theta_a)} \quad (3.6)$$

T_A and T_a are the kinetic energies of particle A and a, P_A and P_a are the relativistic momenta of particle A and a, respectively. θ_a is a scattering angle of particle a. The quantities related to reactants are well known and the quantities related to known product (deuterons) can be determined from the detector. The Q value can be determined from the measured energy and scattering angle of the deuterons by using equation 3.6. Figure 3.15 shows the Q value spectrum for ^{11}Li*(d,d)*^{11}Li' with a deuteron target thickness of 50 μm. This spectrum was converted into excitation spectrum by using

$$E_{exc} = E_{gs} - Q \quad (3.7)$$

where E_{gs} = 0 MeV. Figure 3.16 shows the excitation spectrum. This excitation spectrum was constructed by using all the deuterons selected in Figure 3.9 i.e. all the deuterons detected by YY1-CsI(Tl) detector telescope. However, our reaction of interest, ^{11}Li(d,d')^{11}Li is not the only source of deuterons coming in the detector. The other source of deuterons can be background contribution coming from the Ag foil via fusion-evaporation reactions and the deuteron contribution from non-resonant phase space.

3.4 Background subtraction

3.4.1 Background from the Ag foil

The ^{11}Li beam passes through the Ag foil before it interacts with the solid deuteron target. The reactions in the Ag foil could lead to different reaction channels that can

contribute to *p, d, t* as reaction products, mainly from fusion-evaporation reactions. However, these non-target contributions can be measured using data from ^{11}Li beam on the Ag foil when no solid D_2 target is present. Figure 3.17 shows the no-target excitation spectrum (red) along with the with-target excitation spectrum (blue).

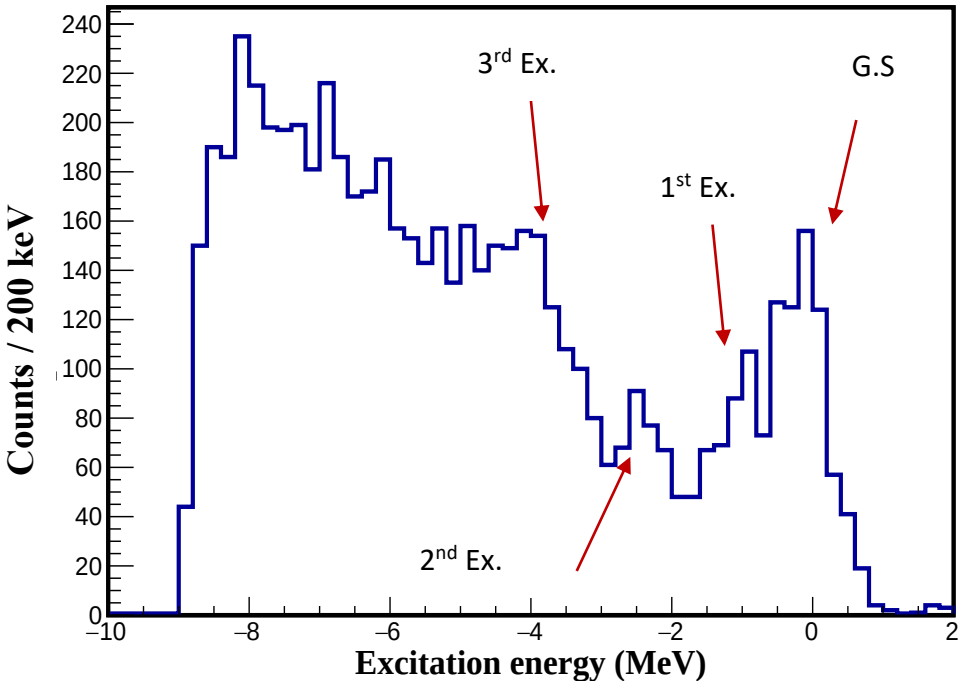

Figure 3.15 Q value spectrum for ^{11}Li*(d,d)*^{11}Li$_{gs}$ and ^{11}Li(*d,d'*)^{11}Li$_{ex}$ with 50 µm D_2 target thickness.

To estimate the contribution coming from reactions in the Ag foil, the measured excitation spectrum without D_2 target was normalized to the ratio of incident beam particles with D_2 target to those without D_2 target i.e.

$$normalization\ factor = \frac{number\ of\ incident\ ^{11}\text{Li}\ particles\ with\ D_2\ target}{number\ of\ incident\ ^{11}\text{Li}\ particle\ without\ D_2\ target} \quad (3.8)$$

normalization factor obtained by using equation 3.8 was 1.67 for 100 µm target and 2.37 for 50 µm target. This normalized background was subtracted from the total excitation spectrum.

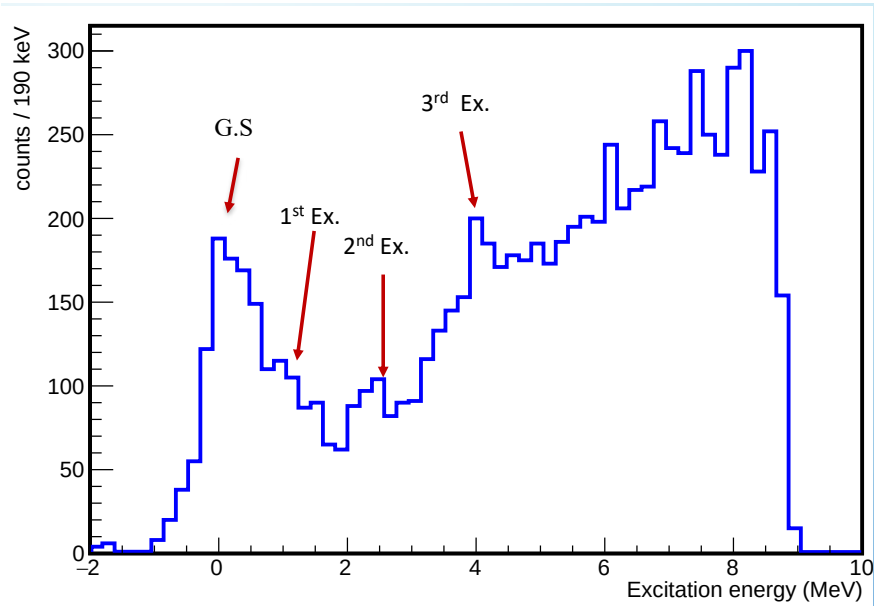

Figure 3.16 Excitation spectrum for ^{11}Li(d,d)^{11}Li$_{gs}$ and ^{11}Li(d,d')^{11}Li$_{ex}$ with 50 μm D_2 target thickness.

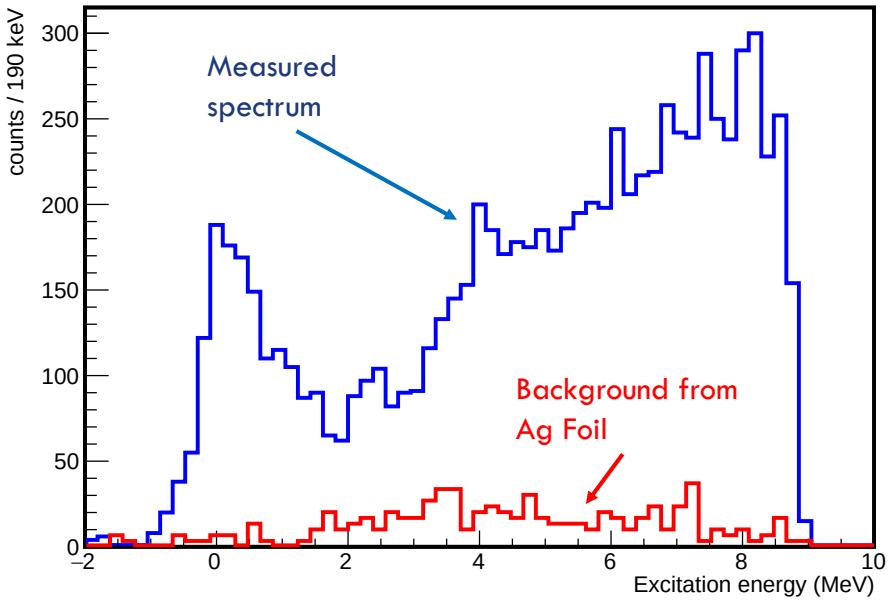

Figure 3.17 Excitation spectrum for ^{11}Li from data with D_2 target thickness of 50 μm (blue) and background contribution (red) from reactions on Ag foil.

3.4.2 Phase space contribution

The reaction of interest in this study is ^{11}Li(d,d'), but there are other reaction channels that are open at this energy which can contribute to our excitation spectrum. The

non-resonant breakup channel reactions are: for three-body $^{11}\mathrm{Li} + d \rightarrow {}^{10}\mathrm{Li} + d + n$, for four-body $^{11}\mathrm{Li} + d \rightarrow {}^{9}\mathrm{Li} + d + n + n$ and for five-body $^{11}\mathrm{Li} + d \rightarrow {}^{8}\mathrm{Li} + d + n + n + n$. The contribution from these different channels was evaluated from the simulation. This non-resonant phase space was simulated considering isotropic emission of the products in the center-of-mass frame. The kinematics of the process was simulated using 'TGenPhasespace', a utility class in ROOT (data analysis framework by CERN), which allows to generate an n-body final state event. The decay of a particle defined as a Lorentz four-momentum into *n-bodies* can be simulated. The contribution from each of the above-mentioned phase space channels is shown in Figure 3.18 along with the measured excitation spectrum. To normalize the background from non-resonant phase space, the sum of these contributions was scaled to the total excitation spectrum through χ^2 minimization. Figure 3.19 represents the total contribution from non-resonant phase space (red) along with the measured excitation spectrum (blue). The phase space excitation spectrum is subtracted from the measured spectrum to obtain the excitation spectrum for our reaction of interest i.e. $^{11}\mathrm{Li}(d,d')^{11}\mathrm{Li}$.

3.5 Extracting resonance states

To find the peak position and width of the newly found resonance, the spectrum needs to be fitted with an appropriate function describing the resonance as well as the bound states together. The bound states have negligible widths that allows us to fit ground state of ^{11}Li with a Gaussian function (only experimental resolution). The width of the resonance

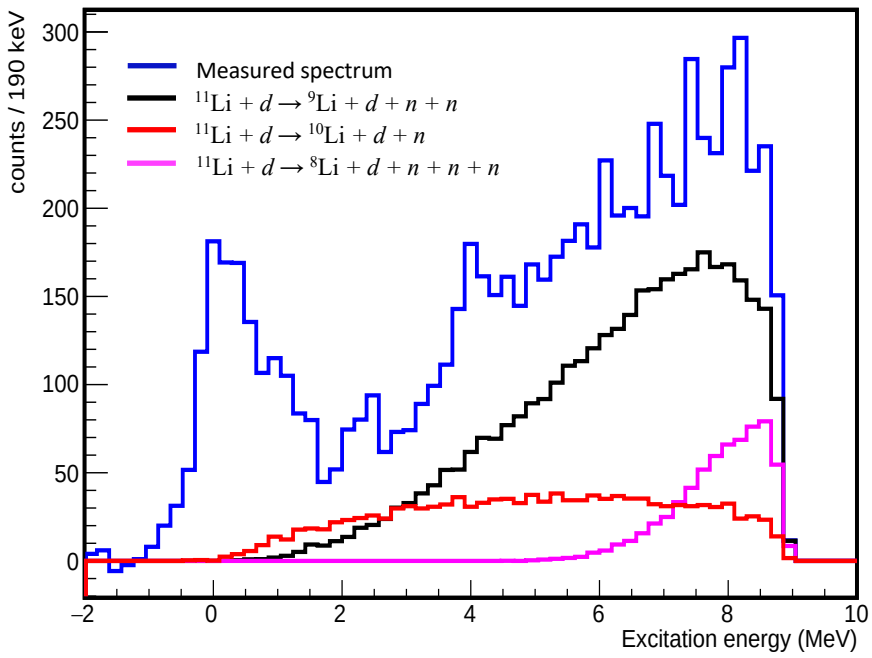

Figure 3.18 The simulated non-resonant phase space contribution from a) $^{11}Li + d \rightarrow {}^{9}Li + d + n + n$ (black), b) $^{11}Li + d \rightarrow {}^{10}Li + d + n$ (red) and c) $^{11}Li + d \rightarrow {}^{8}Li + d + n + n + n$ (magenta) along with measured excitation spectrum (blue) with 50 μm D_2 target thickness.

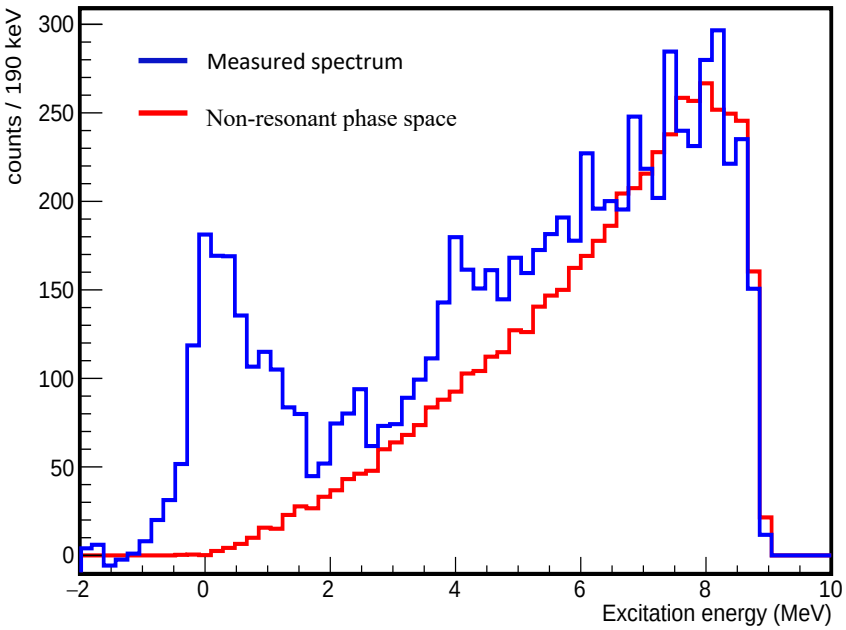

Figure 3.19 The normalized sum of all non-resonant phase space channels (red) along with measured excitation spectrum (blue) with 50 μm D_2 target thickness.

states can be represented by Breit-Wigner distributions. Therefore, the background subtracted excitation spectrum was fitted by using the sum of a Gaussian and three Breit-Wigner distributions with an energy-dependent width folded by the Gaussian experimental resolution (Voigt function). The Voigt function a is three parameter distribution with position (x), natural width (Γ) and resolution (σ). The resolution corresponding to each was obtained using the Monte Carlo simulations, where the natural resonance width of the Breit-wigner functions were set to zero. Therefore, the widths and positions of each function were free parameters while fixing the resolutions. The background subtracted spectrum was fitted by using the above-mentioned functions. Figure 3.20 shows the fitted excitation spectrum. The peak positions for the resonances obtained from fitting were found to be 1.06 ± 0.06 MeV, 2.29 ± 0.04 MeV and 4.01 ± 0.04 MeV. The fit parameters corresponding to each peak are mentioned in Table 3.1.

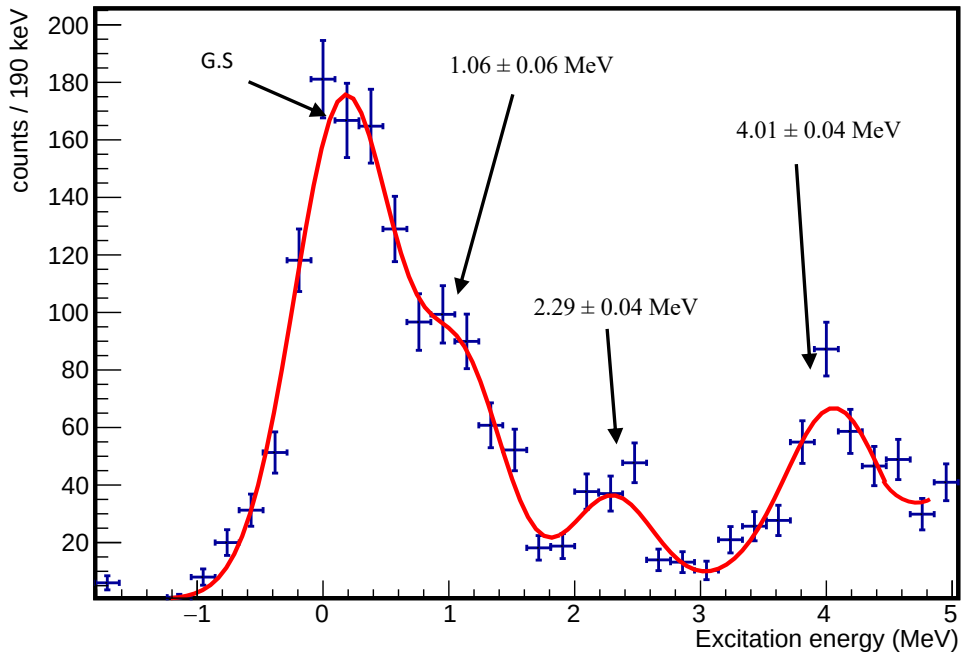

Figure 3.20 Background subtracted measured excitation spectrum for ^{11}Li(d,d') with 50 μm D_2 target thickness.

The FWHM for the resonance peak at 1.06 MeV and 2.29 MeV peak were comparable to the experimental resolutions obtained from the simulations; this shows the observed widths of these resonances were driven the by experimental resolution. However, the resonance at 4.01 MeV shows the natural resonance width of 0.44 ± 0.17 MeV that is extracted by subtracting in quadrature the resolution width from the total width.

Peak position (MeV)	FWHM (MeV)	Resolution (MeV)
0.00 ± 0.06	0.88 ± 0.04	0.87 ± 0.01
1.06 ± 0.06	0.77 ± 0.02	0.78 ± 0.02
2.29 ± 0.04	0.76 ± 0.02	0.78 ± 0.02
4.01 ± 0.04	1.25 ± 0.03	0.72 ± 0.02

Table 3.1 Table listing the fitting parameters obtained from Figure 3.21 for the ^{11}Li resonance states

The fitting of excitation spectrum with 50 μm target thickness data gave the information about the peak position, natural widths and relative amplitude of each peak. This information was used to simulate the excitation spectrum with 100 μm target thickness. The simulated excitation spectrum with 100 μm target thickness is shown in Figure 3.21. The experimental resolution with 100 μm target thickness corresponding to each resonance state along with ground state is listed in Table 3.2. It can be seen from the table 3.1 and table 3.2 that the resolution with 100 μm target was slightly poor than the 50 μm target.

Peak position (MeV)	Resolution (MeV)
G.S	0.92 ± 0.01
1.06 ± 0.06	0.84 ± 0.01
2.29 ± 0.04	0.82 ± 0.01
4.01 ± 0.04	0.76 ± 0.02

Table 3.2 Table listing the resolution corresponding to each state expected with a 100 μm target thickness as obtained from simulation.

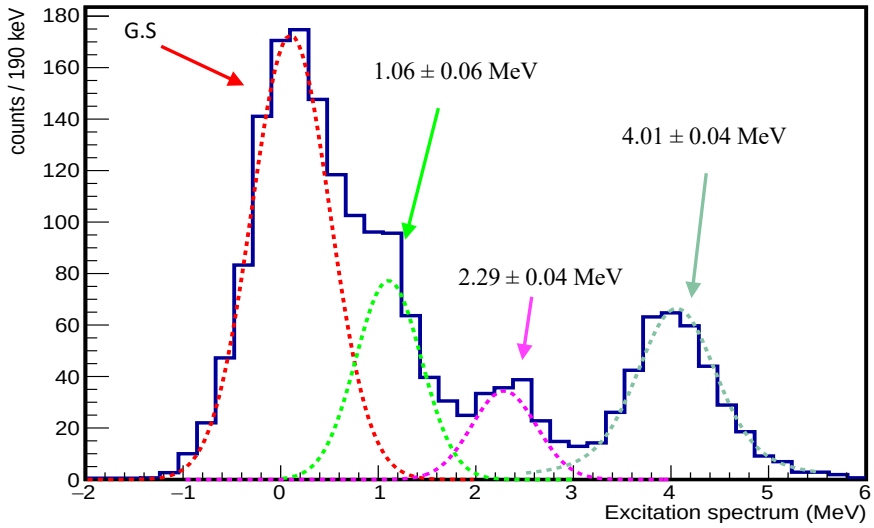

Figure 3.21 Simulated excitation spectrum for ^{11}Li(*d*,*d'*) with 100 μm D_2 target thickness.

The non-resonant phase space was simulated for the 100 μm target thickness as well by using the method explained in section 3.4.2 and is shown in Figure 3.22. The measured excitation spectrum with the 100 μm target thickness is shown in Figure 3.23. The total simulated excitation spectrum was compared to the measured excitation spectrum with the 100 μm target data. Figure 3.24 shows the simulated excitation spectrum (blue) overlaid

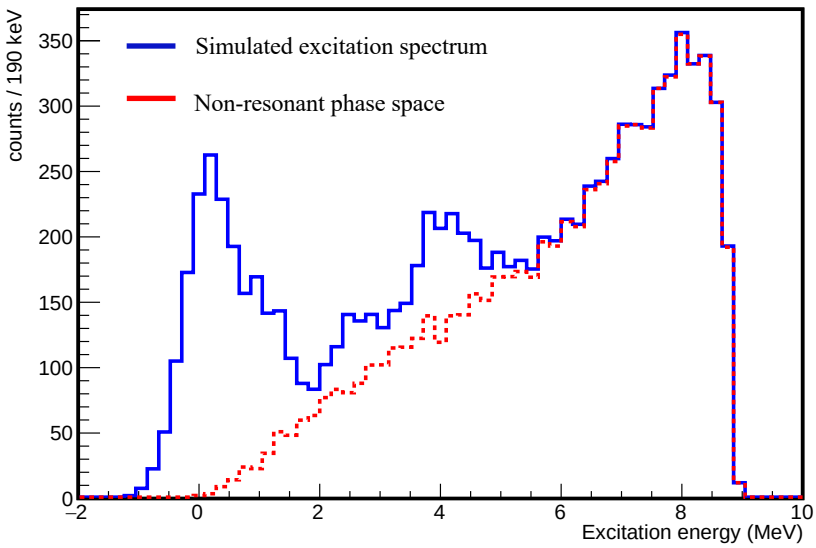

Figure 3.22 Simulated non-resonant phase space contribution (red) along with total simulated excitation spectrum (blue) for ^{11}Li(*d,d'*) with 100 μm target thickness.

with the measured excitation spectrum (red) with the 100 μm target. The peak observed at 2.29 ± 0.04 MeV is not clearly visible with the 100 μm target. This seems to be due to lack of the resolution with the 100 μm target together with the fact that the peak at 4 MeV is very broad. It is clear from the Figure 3.24 that the two spectra are in very good agreement with each other supporting the observed resonances in the spectrum with 50 μm target thickness as being excited states of ^{11}Li. As it is observed in Figure 3.24 the simulation is not within very good agreement with the measured spectrum around 5 MeV to 7 MeV range. This disagreement is may be due to other resonances above 5 MeV which are not included in our simulation.

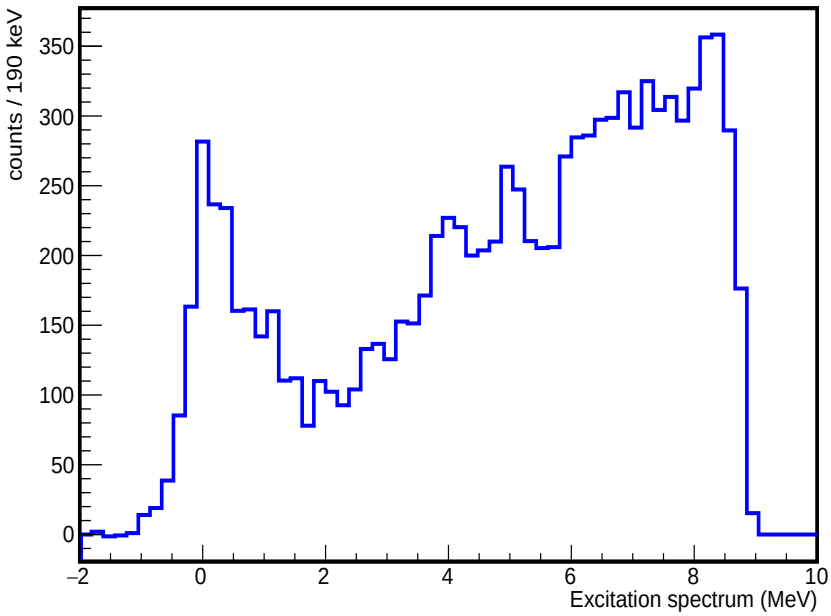

Figure 3.23 Measured excitation spectrum for ^{11}Li(*d*,*d*′) reaction with 100 μm target thickness.

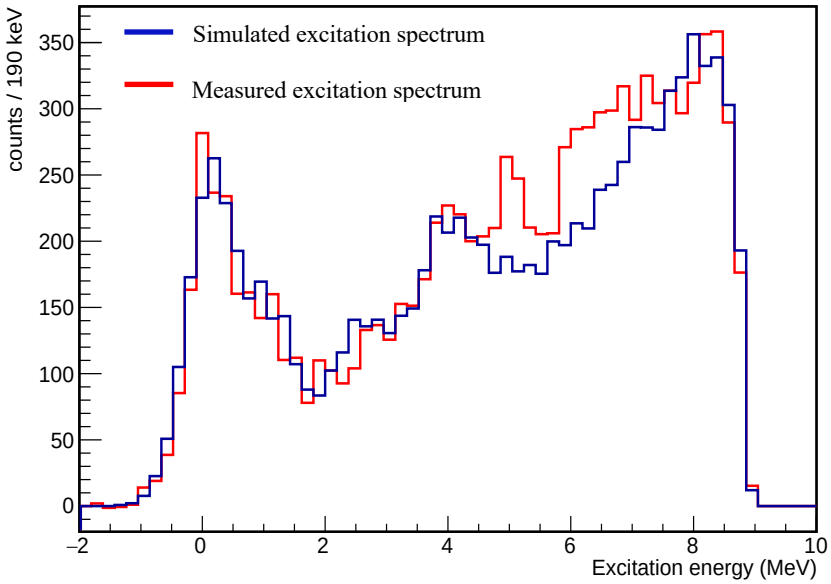

Figure 3.24 The simulated excitation spectrum (blue) compared to the measured excitation spectrum (red) with the 100 μm D_2 target.

Chapter 4

Results and Conclusion

In the previous chapter, the excitation spectrum is presented for data collected with two different deuteron target thickness i.e. 100 μm and 50 μm. Three resonances were observed along with ground state. The first excited state at 1.06 ± 0.06 MeV was observed. This state can be identified as the state confirmed at 1.03 ± 0.03 MeV via ^{11}Li(*d,d*) by Ref. [52] and that observed by Gornov *et al.*[46] at 1.02 ± 0.07 MeV by ^{14}C *(π^-, pd)* reaction.

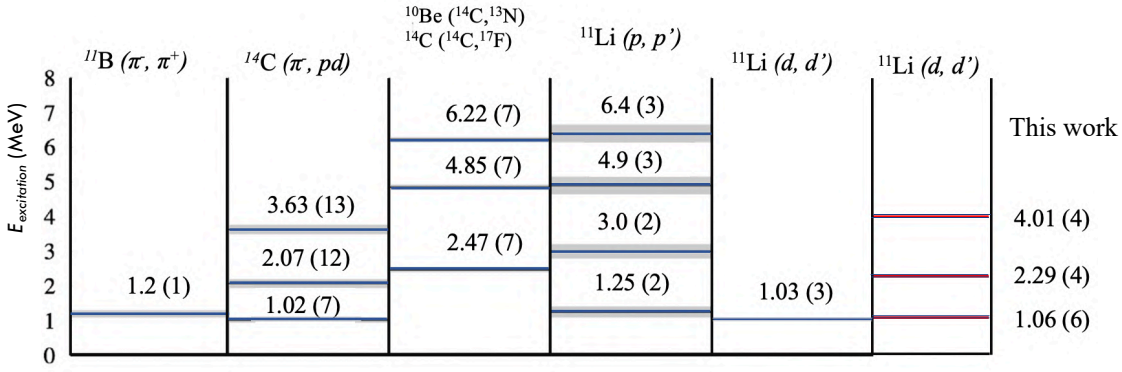

Figure 4.1 Reported resonance states of ^{11}Li. The grey bars are uncertainties in excitation energy. The resonances observed from our study are presented in red.

The second resonance state in the excitation spectrum is observed at 2.29 ± 0.04 MeV. This state can be compared to state observed via ^{14}C *(π^-, pd)* reaction at 2.07 ± 0.12 MeV within 2σ uncertainties. However, this state might not be populated by proton inelastic scattering [45]. In contrast, in a study of ^{10}Be (^{14}C,^{13}N) and ^{14}C (^{14}C,^{17}F) reactions, Bohlen *et al.* [44] do not observe a state at 1.06 MeV, but observed states at 2.47 ± 0.07, 4.85 ± 0.07 MeV, and 6.22 ± 0.07 MeV. Our second resonance state can be identified with the 2.47 ± 0.07 MeV state reported in this nucleon transfer reaction within 2σ uncertainties.

The resonance observed in our spectrum at 4.01 ± 0.04 MeV is potentially a new resonance. This resonance might not be populated by previously reported experiments. The width of this state wase observed to be 0.44 ± 0.17 MeV.

The final goal of this study is to assign the properties of these states like spin from the multipolarity of excitation. The angular distribution for these resonances will be determined by using the relation for differential cross-section

$$\frac{d\sigma}{d\Omega} = \left[\frac{N^{sc}}{N^{in}}\right] \times \left[\frac{1}{\rho t}\frac{M_t}{N_A}\frac{1}{d\Omega}\right] \qquad (4.1)$$

where N^{sc} and N^{in} are the number of scattered particles and incident particles respectively. M_t, ρ and t are molar mass, density, and thickness of solid D_2 target respectively. N_A and $d\Omega$ are the Avogadro's number and solid angle respectively. Out of these various quantities M_t, ρ & N_A are constant, target thickness 't' is known at each instant and N^{in} can be estimated from IC counts. N^{sc} can be determined by counting the number of deuterons in a detected by detector in each angular bin.

To get the spin of the state, angular distributions will be interpreted in the framework of a one-step Distorted Wave Born Approximation (DWBA) calculation. The best fitted calculated angular distribution with our measured angular distribution for ground state that will provide the optical potential parameters. By using these potential parameters, the inelastic scattering angular distribution will be calculated for different multipolarities. The calculations that best fit with the measurements help to get the multipolarity of excitation.

As it is known that the conventional shell model and Hartree-Fock calculations are successfully used to describe the properties of nuclei, both close to stability and around shell closures. When coming near the nuclear limits (driplines), these approaches need to be adjusted, to take into account for continuum effects, e.g., for higher masses (A > 100) the Hartree-Fock-Bogoliubov method allows for interactions between bound and continuum states, showing a significant change of the shell structure [58]. However, these mean-field approaches are not very successful when the halo appears, because the field felt by the halo nucleons is different from the field felt by the inert core nucleons: the halo binding is too weak to allow a mean-field description. The failure of our traditional approaches (shell model and Hartree-Fock calculations) can be seen from the different experiments; it is observed that the orbitals can shift in halo nuclei to alter the conventional magic numbers (shell closures) [59,60]. This study will help physicists to add corrections to these approaches and give us more insight on nuclear structure near the driplines.

Summary

A study of the excitation spectrum of the two-neutron halo nucleus ^{11}Li was carried out at the IRIS facility using the ^{11}Li(*d,d'*) reaction with beam energy 7.3*A* MeV with two different deuteron target thicknesses (50 μm and 100 μm) were used in experiment. The excitation spectrum shows three prominent resonances. The first excited state is observed at 1.06 ± 0.06 MeV and second excited state is observed at 2.29 ± 0.04 MeV which are consistent with previously reported resonances. A potentially new resonance was observed at 4.01 ± 0.04 MeV with resonance width of 0.44 ± 0.17 MeV. The spectrum will be further studied to extract characteristics of these resonance states.

References

1. Janssens, R. V. (2009). Unexpected doubly magic nucleus. *Nature,459*(7250), 1069-1070. doi:10.1038/4591069a
2. Volya, A., & Tchuvilsky, Y. M. (2015). Nuclear clustering using a modern shell model approach. *Physical Review C,91*(4). doi:10.1103/physrevc.91.044319
3. Ericson, Torleif. "The Statistical Model and Nuclear Level Densities." *Advances in Physics*, vol. 9, no. 36, 1960, pp. 425–511., doi:10.1080/00018736000101239.
4. Hodgson, P E. "The Nuclear Optical Model." *Reports on Progress in Physics*, vol. 34, no. 2, 1971, pp. 765–819., doi:10.1088/0034-4885/34/2/306.
5. Eden, R.j. "Nuclear Models." *Progress in Nuclear Physics*, 2013, pp. 26–51., doi:10.1016/b978-1-4831-9887-3.50006-2.
6. Rutherford, E. (1914). LVII. The structure of the atom. *The London, Edinburgh, and Dublin Philosophical Magazine and Journal of Science,27*(159), 488-498. doi:10.1080/14786440308635117
7. Bohr, N. (1913). I. On the constitution of atoms and molecules. *The London, Edinburgh, and Dublin Philosophical Magazine and Journal of Science,26*(151), 1-25. doi:10.1080/14786441308634955
8. Salpeter, E. E. (1997). Models and Modelers of Hydrogen. *American Journal of Physics,65*(9), 933-934. doi:10.1119/1.18691
9. Caurier, E., Martínez-Pinedo, G., Nowacki, F., Poves, A., & Zuker, A. P. (2005). The shell model as a unified view of nuclear structure. *Reviews of Modern Physics,77*(2), 427-488. doi:10.1103/revmodphys.77.427

10. Mayer, M. G. (1949). On Closed Shells in Nuclei. II. *Physical Review,75*(12), 1969-1970. doi:10.1103/physrev.75.1969

11. https://www.nndc.bnl.gov

12. Hansen, P. G., Jensen, A. S., & Jonson, B. (1995). Nuclear Halos. *Annual Review of Nuclear and Particle Science,45*(1), 591-634. doi:10.1146/annurev.ns.45.120195.003111

13. Hansen, P. G., & Jonson, B. (1987). The Neutron Halo of Extremely Neutron-Rich Nuclei. *Europhysics Letters (EPL),4*(4), 409-414. doi:10.1209/0295-5075/4/4/005

14. Demyanova, A. S., Ogloblin, A. A., Danilov, A. N., Belyaeva, T. L., Goncharov, S. A., & Trzaska, W. (2016). Proton halo in the 13N nucleus. *JETP Letters,104*(8), 526-530. doi:10.1134/s0021364016200108

15. Canham, D. L., & Hammer, H. -. (2008). Universal properties and structure of halo nuclei. *The European Physical Journal A,37*(3). doi:10.1140/epja/i2008-10632-4

16. Riisager, K. (1994). Nuclear halo states. *Reviews of Modern Physics,66*(3), 1105-1116. doi:10.1103/revmodphys.66.1105

17. Zhukov, M., Danilin, B., Fedorov, D., Bang, J., Thompson, I., & Vaagen, J. (1993). Bound state properties of Borromean halo nuclei: 6He and 11Li. *Physics Reports,231*(4), 151-199. doi:10.1016/0370-1573(93)90141-y

18. Jensen, A. S., Riisager, K., Fedorov, D. V., & Garrido, E. (2004). Structure and reactions of quantum halos. *Reviews of Modern Physics,76*(1), 215-261. doi:10.1103/revmodphys.76.215

19. Tanaka, K., Yamaguchi, T., Suzuki, T., Ohtsubo, T., Fukuda, M., Nishimura, D., . . . Yoshitake, M. (2010). Observation of a Large Reaction Cross Section in the Dripline NucleusC22. *Physical Review Letters,104*(6). doi:10.1103/physrevlett.104.062701

20. Pfützner, M., Karny, M., Grigorenko, L. V., & Riisager, K. (2012). Radioactive decays at limits of nuclear stability. *Reviews of Modern Physics,84*(2), 567-619. doi:10.1103/revmodphys.84.567

21. Amorim, A. E., Frederico, T., & Tomio, L. (1997). Universal aspects of Efimov states and light halo nuclei. *Physical Review C,56*(5). doi:10.1103/physrevc.56.r2378

22. Horiuchi, W., & Suzuki, Y. (2006). C22: Ans-wave two-neutron halo nucleus. *Physical Review C,74*(3). doi:10.1103/physrevc.74.034311

23. Yamashita, M. T., Frederico, T., & Tomio, L. (2008). Trajectory of virtual, bound and resonant Efimov states. *Few-Body Systems,44*(1-4), 191-193. doi:10.1007/s00601-008-0288-5

24. Mazumdar, I., Rau, A. R., & Bhasin, V. S. (2006). Efimov States and their Fano Resonances in a Neutron-Rich Nucleus. *Physical Review Letters,97*(6). doi:10.1103/physrevlett.97.062503

25. Mazumdar, I., & Bhasin, V. (1997). Efimov effect in the nuclear halo 14Be nucleus. *Physical Review C,56*(1). doi:10.1103/physrevc.56.r5

26. Tanihata, I. (1996). Neutron halo nuclei. *Journal of Physics G: Nuclear and Particle Physics,22*(2), 157-198. doi:10.1088/0954-3899/22/2/004

27. Bagchi, S., Kanungo, R., Tanaka, Y., Geissel, H., Doornenbal, P., Horiuchi, W., . . . Yoshida, K. (2020). Two-Neutron Halo is Unveiled in ^{29}F. *Physical Review Letters,124*(22). doi:10.1103/physrevlett.124.222504

28. Riisager, K., Jensen, A., & Møller, P. (1992). Two-body halos. *Nuclear Physics A,548*(3), 393-413. doi:10.1016/0375-9474(92)90691-c

29. Tanihata, I., Hamagaki, H., Hashimoto, O., Shida, Y., Yoshikawa, N., Sugimoto, K., . . . Takahashi, N. (1985). Measurements of Interaction Cross Sections and Nuclear Radii in the Lightp-Shell Region. *Physical Review Letters,55*(24), 2676-2679. doi:10.1103/physrevlett.55.2676

30. Arnold, E., Bonn, J., Gegenwart, R., Neu, W., Neugart, R., Otten, E., . . . Wendt, K. (1987). Nuclear spin and magnetic moment of ^{11}Li. *Physics Letters B,197*(3), 311-314. doi:10.1016/0370-2693(87)90390-x

31. Kobayashi, T., Shimoura, S., Tanihata, I., Katori, K., Matsuta, K., Minamisono, T., . . . Wieman, H. (1989). Electromagnetic dissociation and soft giant dipole resonance of the neutron-dripline nucleus ^{11}Li. *Physics Letters B,232*(1), 51-55. doi:10.1016/0370-2693(89)90557-1

32. Ieki, K., Sackett, D., Galonsky, A., Bertulani, C. A., Kruse, J. J., Lynch, W. G., . . . Humphrey, D. L. (1993). Coulomb dissociation of ^{11}Li. *Physical Review Letters,70*(6), 730-733. doi:10.1103/physrevlett.70.730

33. Shimoura, S., Nakamura, T., Ishihara, M., Inabe, N., Kobayashi, T., Kubo, T., . . . Watanabe, Y. (1995). Coulomb dissociation reaction and correlations of two halo neutrons in 11Li. *Physics Letters B,348*(1-2), 29-34. doi:10.1016/0370-2693(95)00131-4

34. Kobayashi, T., Yamakawa, O., Omata, K., Sugimoto, K., Shimoda, T., Takahashi, N., & Tanihata, I. (1988). Projectile Fragmentation of the Extremely Neutron-Rich Nucleus ^{11}Li at 0.79 GeV/nucleon. *Physical Review Letters,60*(25), 2599-2602. doi:10.1103/physrevlett.60.2599

35. Borge, M., Deding, J., Hansen, P., Jonson, B., Pinedo, G. M., Møller, P., . . . Tengblad, O. (1993). Beta-decay to the proton halo state in ^{17}F. *Physics Letters B,317*(1-2), 25-30. doi:10.1016/0370-2693(93)91564-4

36. Borge, M. J., Hansen, P. G., Johannsen, L., Jonson, B., Nilsson, T., Nyman, G., . . . Wilhelmsen, K. (1991). Super-allowed beta decay of nuclei at the dripline. *Zeitschrift Für Physik A Hadrons and Nuclei,340*(3), 255-261. doi:10.1007/bf01294673

37. Korsheninnikov, A., & Kobayashi, T. (1994). Main mechanisms in fragmentation of the exotic nucleus ^{6}He. *Nuclear Physics A,567*(1), 97-110. doi:10.1016/0375-9474(94)90728-5

38. Orr, N. A., Anantaraman, N., Austin, S. M., Bertulani, C. A., Hanold, K., Kelley, J. H., . . . Winger, J. A. (1992). Momentum distributions of ^{9}Li fragments following the breakup ofLi11. *Physical Review Letters,69*(14), 2050-2053. doi:10.1103/physrevlett.69.2050

39. Rohlf, J. W., & Collings, P. J. (1994). Modern Physics from α to Z°. *Physics Today,47*(12), 62-63. doi:10.1063/1.2808751

40. Krane, K. S., & Halliday, D. (1988). *Introductory nuclear physics*. New York: Wiley.

41. Klapisch, R., Thibault-Philippe, C., Detraz, C., Chaumont, J., Bernas, R., & Beck, E. (1969). Half-Life of ^{11}Li, of ^{27}Na, and of the New Isotopes ^{28}Na, ^{29}Na, ^{30}Na, and ^{31}Na Produced in High-Energy Nuclear Reactions. *Physical Review Letters,23*(12), 652-655. doi:10.1103/physrevlett.23.652

42. Smith, M., Brodeur, M., Brunner, T., Ettenauer, S., Lapierre, A., Ringle, R., . . . Dilling, J. (2008). First Penning-Trap Mass Measurement of the Exotic Halo Nucleus ^{11}Li. *Physical Review Letters,101*(20). doi:10.1103/physrevlett.101.202501

43. Kobayashi, T. (1992). Projectile fragmentation of exotic nuclear beams. *Nuclear Physics A,538*, 343-352. doi:10.1016/0375-9474(92)90784-h

44. Bohlen, H. G., Kalpakchieva, R., Aleksandrov, D. V., Gebauer, B., Grimes, S. M., Kirchner, T., . . . Wilpert, T. (1995). Spectroscopy of excited states of ^{11}Li. *Zeitschrift Für Physik A Hadrons and Nuclei,351*(1), 7-8. doi:10.1007/bf01292778

45. Korsheninnikov, A. A., Nikolskii, E. Y., Kobayashi, T., Ozawa, A., Fukuda, S., Kuzmin, E. A., . . . Yoshida, K. (1996). Spectroscopy of the halo nucleus ^{11}Li by an experimental study ofLi11 pcollisions. *Physical Review C,53*(2). doi:10.1103/physrevc.53.r537

46. Gornov, M. G., Gurov, Y., Lapushkin, S., Morokhov, P., Pechkurov, V., Pedlar, T. K., . . . Zhao, D. (1998). Excited States of ^{11}Li. *Physical Review Letters,81*(20), 4325-4328. doi:10.1103/physrevlett.81.4325

47. Korsheninnikov, A. A., Kuzmin, E. A., Nikolskii, E. Y., Bochkarev, O. V., Fukuda, S., Goncharov, S. A., . . . Yoshida, K. (1997). L=1 Excitation in the Halo Nucleus ^{11}Li. *Physical Review Letters,78*(12), 2317-2320. doi:10.1103/physrevlett.78.2317

48. Zhukov, M, et al. "Fingerprints of a Possible Low-Lying Resonance in ^{11}Li." *Journal of Physics G: Nuclear and Particle Physics*, vol. 20, no. 1, 1994, pp. 201–213., doi:10.1088/0954-3899/20/1/020.

49. Nakamura, T., Vinodkumar, A. M., Sugimoto, T., Aoi, N., Baba, H., Bazin, D., . . . Yoneda, K. (2006). Observation of Strong Low-Lying E1 Strength in the Two-Neutron Halo Nucleus ^{11}Li. *Physical Review Letters,96*(25). doi:10.1103/physrevlett.96.252502

50. Tanaka, J., Kanungo, R., Alcorta, M., Aoi, N., Bidaman, H., Burbadge, C., . . . Tanihata, I. (2017). Halo-induced large enhancement of soft dipole excitation of ^{11}Li observed via

proton inelastic scattering. *Physics Letters B,774*, 268-272. doi:10.1016/j.physletb.2017.09.079

51. Sanetullaev, A., et al. “Investigation of the Role of 10Li Resonances in the Halo Structure of 11Li through the ^{11}Li(*p,d*)^{10}Li Transfer Reaction.” *Physics Letters B*, vol. 755, 2016, pp. 481–485., doi:10.1016/j.physletb.2016.02.060.
52. Kanungo, R., Sanetullaev, A., Tanaka, J., Ishimoto, S., Hagen, G., Myo, T., . . . Wang, Z. (2015). Evidence of Soft Dipole Resonance inLi11with Isoscalar Character. *Physical Review Letters,114*(19). doi:10.1103/physrevlett.114.192502
53. *https://www.triumf.ca/research-program/research-facilities/isac-facilities*
54. Kanungo, R. (2013). IRIS: The ISAC charged particle reaction spectroscopy facility for reaccelerated high-energy ISOL beams. *Hyperfine Interactions,225*(1-3), 235-240. doi:10.1007/s10751-013-0904-8
55. *http://www.micronsemiconductor.co.uk/product/yy1/*
56. *http://www.micronsemiconductor.co.uk/product/s3/*
57. *https://www.mesytec.com/products/nuclear-physics/MSCF-16.html*
58. Dobaczewski, J., Hamamoto, I., Nazarewicz W.,, and A. Sheikh, J., Nuclear shell structure at particle drip lines, *Physical Review Letters*, 72 (1994), pp. 981–984.
59. Tran, D.T. et al. Evidence for prevalent $Z = 6$ magic number in neutron-rich carbon isotopes. Nature communications 9 (1): 1-7, 2018
60. XiangSun, X. et al., Shrunk halo and quenched shell gap at $N = 16$ in ^{22}C: Inversion of *sd* states and deformation effects. *Physics Letters B*, vol. 785, 2018, pp. 530-535